Quantification of solid fuel combustion and aqueous chemistry contributions to secondary organic aerosol during wintertime haze events in Beijing

Yandong Tong[1], Veronika Pospisilova[1,a], Lu Qi[1], Jing Duan[2], Yifang Gu[2], Varun Kumar[1], Pragati Rai[1], Giulia Stefenelli[1], Liwei Wang[1], Ying Wang[2], Haobin Zhong[2], Urs Baltensperger[1], Junji Cao[2], Ru-Jin Huang[2], Andre S. H. Prevot[1], and Jay G. Slowik[1]

[1]Laboratory of Atmospheric Chemistry, Paul Scherrer Institute (PSI), 5232 Villigen, Switzerland

[2]Key Lab of Aerosol Chemistry & Physics, Institute of Earth Environment, Chinese Academy of Sciences, Xi'an, China

[a]now at: Tofwerk AG, Uttigenstrasse 22, 3600 Thun, Switzerland

Correspondence: J. G. Slowik (jay.slowik@psi.ch)

Abstract: In recent years, intense haze events in megacities such as Beijing have received significant study. Although secondary organic aerosol (SOA) has been identified as a major contributor to such events, knowledge of its sources and formation mechanisms remains uncertain. We investigate this question through the first field deployment of the extractive electrospray ionisation time-of-flight mass spectrometer (EESI-TOF) in Beijing, together with an Aerodyne long time-of-flight aerosol mass spectrometer (L-TOF AMS). Measurements were performed during autumn and winter 2017, capturing the transition from non-heating to heating seasons. Source apportionment resolved four factors related to primary organic aerosols (traffic, cooking, biomass burning, and coal combustion), as well as four related to secondary organic aerosol (SOA). Of the SOA factors, two were related to solid fuel combustion (SFC), one to SOA generated from aqueous chemistry, and one to mixed/indeterminate sources. The SFC factors were identified from spectral signatures corresponding to aromatic oxidation products, while the aqueous SOA factor was characterised by signatures of small organic acids and diacids, and unusually low CO^+/CO_2^+ fragment ratios measured by the AMS. Solid fuel combustion was the dominant source of SOA during the heating season. However, a comparably intense haze event was also observed in the non-heating season, and was dominated by the aqueous SOA factor. Aqueous chemistry was promoted by the combination of high relative humidity and air masses passing over high NO_x regions to the south and east of Beijing, leading to high particulate nitrate. The resulting high liquid water content was highly correlated with the concentration of the aqueous SOA factor. These results highlight the strong compositional variability between different haze events, indicating the need to consider multiple formation pathways and precursor sources to describe SOA during intense haze events in Beijing.

1. Introduction

Atmospheric aerosols negatively affect human health (Liu et al., 2017a; Krapf et al., 2017; Beelen et al., 2014; Laden et al., 2006; Pope et al., 2002), visibility (Chow et al., 2002), and urban air quality (Fenger, 1999; Mayer, 1999) on local and regional scales. Aerosols are also linked to the most important uncertainties related to global radiation balance and climate change (Myhre et al., 2014; Penner et al., 2011; Forster et al., 2007; Lohmann and Feichter, 2005). Therefore, understanding of aerosol chemical composition, sources, and evolution is fundamental to the development of appropriate mitigation policies. Organic aerosol (OA) is a major component of atmospheric aerosol and contributes significantly to the total aerosol mass (Jimenez et al., 2009). OA sources are typically classified as either primary organic aerosol (POA), which is directly emitted from sources such as fossil fuel combustion, industrial emissions, biomass burning and cooking emissions, or secondary organic aerosol (SOA), which is produced by atmospheric oxidation of volatile organic compounds (VOCs), yielding lower-volatility products that can subsequently partition to the particle phase. Globally, SOA accounts for approximately from 50 % to 90 % of total OA, with the predominant fraction of SOA (90 %) from oxidation of biogenic VOCs and only 10 % of SOA from anthropogenic VOCs (Jimenez et al., 2009; Hallquist et al., 2009). However, studies have shown that SOA production and its properties can be affected by the interaction between biogenic and anthropogenic VOCs. Apart from huge uncertainties in production and properties, SOA can also exert serious health effects, including protein and DNA damage caused by reactive oxygen species (ROS) induced from SOA (Reuter et al., 2010; Li et al., 2003; Halliwell and Cross, 1994). Recent studies indicate that the ROS content of SOA is source-dependent, suggesting health risks may likewise be source-dependent, highlighting the importance of OA source identification and quantification (Daellenbach et al., 2020; Zhou et al., 2018). Previous studies have been relatively successful in quantitatively linking POA to its sources, However, quantification of SOA sources and/or formation pathways is much more challenging (Qi et al., 2019; Stefenelli et al., 2019; Xu et al., 2019; Elser et al., 2016; Sun et al., 2016a; Sun et al., 2013), because SOA consists of thousands of multifunctional, highly oxygenated compounds, including high molecular weight species and oligomers, which are difficult to measure using traditional instrumentation. Therefore, the effects of individual SOA sources on health and climate remain poorly constrained.

Fine aerosol pollution is a major public health concern in many megacities, highlighting the need for efficient mitigation strategies informed by a detailed assessment of POA and SOA sources. Beijing is an area of particular interest, due to the frequency of extreme haze events in northern China (An et al., 2019) and a rapidly changing pollution landscape in response to the "Atmospheric Pollution Prevention and Control Action Plan" implemented in 2013 by the Chinese government. This initiative targeted selected anthropogenic emissions sources, reducing annual mean $PM_{2.5}$ concentration by ~30% between 2013 and 2017 (Xinhuanet, 2018), although annual concentrations remain much higher than both national air quality standards and WHO guidelines. As a result, numerous studies have investigated the composition and sources of $PM_{2.5}$ in Beijing (Duan et al., 2020; Duan et al., 2019; Xu et al., 2019; Zhao et al., 2019; Äijälä et al., 2017; Elser et al., 2016; Hu et al., 2016; Sun et al., 2016a; Huang et al., 2014; Zhang et al., 2014; Sun et al., 2013), with most online source apportionment studies utilising aerosol mass spectrometers (AMS). These studies have successfully identified POA sources, with dominant winter sources including coal combustion (10 to 30%), biomass burning (9 to 18%), traffic (9 to 18%), and cooking (12 to 20%). In contrast, although SOA typically comprises 35 to 70% of Beijing OA, far less is known about its sources and formation processes. In summer, Bryant et al. (2020) found the isoprene-derived SOAs are strongly controlled by anthropogenic NO_x and sulphate aerosols via offline-filter analysis. Wang et al. (2019) discussed the factors that influence the formation of secondary nitro-aromatic compounds under high NO_x concentration and aromatic precursor concentrations. Modeling studies also established links between atmospheric oxidising capacity and SOA formation (Feng et al., 2019), and suggested an influence of heterogeneous HONO and primary residential emission in SOA formation in winter (Xing et al., 2019). However, apportionment of SOA to specific sources has not yet been achieved, with online source apportionment studies (using AMS) reporting either a single SOA factor (denoted oxygenated organic aerosol, OOA), or two factors distinguished by the extent of oxygenation (less oxygenated OOA, LO-OOA, and more oxygenated OOA, MO-OOA) (Xu et al., 2019; Elser et al., 2016; Sun et al., 2016a; Sun et al., 2013).

Limitations in SOA source apportionment are directly tied to limitations of the measuring instruments. For the Aerodyne aerosol mass spectrometer (AMS), a trade-off exists between quantification and time resolution vs. chemical resolution. Quantification and time resolution are facilitated by high temperature vaporisation. which induces significant thermal decomposition and ionisation-induced fragmentation (DeCarlo et al., 2006). This decreases chemical resolution, particularly for the multifunctional and highly oxygenated molecules of which SOA is comprised (e.g., multifunctional acids, peroxides, organonitrates, organosulphates, oligomers), thereby hindering SOA source apportionment. To avoid thermal decomposition, the CHARON PTR-MS uses a lower temperature vaporisation scheme, but the proton transfer reaction ionisation scheme is sufficiently energetic to cause extensive fragmentation of typical SOA molecules (Muller et al., 2017; Eichler et al., 2015). To reduce ionisation-induced fragmentation, several semi-continuous measurement techniques have also been developed, e.g., Thermal Desorption Aerosol GC/MS-FID (TAG) by Williams et al. (2006), and Filter Inlet for Gases and AEROsols chemical ionisation time-of-flight mass spectrometer (FIGAERO-CIMS) by Lopez-Hilfiker et al. (2014). Although these instruments have lower thermal decomposition and better chemical resolution, like offline filter sampling they are subject to reaction/vaporisation processes on the collection substrate and decreased time resolution. Alternatively, offline filter analysis has some advantages, including 1) the possibility to apply a wide variety of analytical techniques, which can maximise the chemical information retrieved for the analysed fraction; and 2) low cost and maintenance requirements for filter sampling, which in turn facilitates 3) practicality of measurements with wide spatial and temporal coverage. However, it also has some drawbacks, including 1) low time resolution incapable of capturing characteristic timescales of certain OA sources and/or ageing and formation processes, 2) artefacts due to adsorption, evaporation, and chemical reactions during sample collection, storage, and/or transfer (Ge et al., 2012; Huang et al., 2010; Hildebrandt et al., 2010; Hallquist et al., 2009), and 3) the analysable OA faction may vary significantly between different techniques.

To better investigate SOA sources and/or formation processes, an instrument that can resolve aerosol chemical composition was recently developed at the Paul Scherrer Institute (PSI). The extractive electrospray ionisation time-of-flight mass spectrometer (EESI-TOF) utilises a soft ionisation technique with minimal thermal energy transfer to the analyte molecules. This yields online, near-molecular-level (i.e., molecular formulae) measurement of organic aerosol composition with high time resolution (seconds) without thermal decomposition or ionisation-induced fragmentation (Lopez-Hilfiker et al., 2019). Operating principles are discussed in detail in section 2.2.1. Two recent source apportionment studies in Zurich using an EESI-TOF, together with an AMS, successfully resolved several SOA factors and quantified the processes governing SOA concentrations for summer and winter (Qi et al., 2019; Stefenelli et al., 2019). These studies confirm that EESI-TOF and AMS are highly complementary, with the AMS providing robust quantification but limited chemical resolution, and the EESI-TOF providing a linear but hard-to-quantify response with high chemical resolution. The combined measurements, therefore, have the potential to provide quantitative, real-time measurements of organic aerosol composition with high chemical resolution.

Here we present AMS and EESI-TOF measurements in Beijing from late September to mid-December 2017. This campaign captures distinct characteristics of the non-heating season and heating season, which begins on 15 November. An integrated source apportionment analysis of AMS and EESI-TOF data is performed to characterise the sources and physicochemical processes governing SOA composition.

2. Methodologies

2.1 Measurement campaign

Beijing is the capital city of China PR and one of the most populated cities in the world, with more than 20 million inhabitants. It is located at the northwestern end of the North China Plain and bordered by the Yan Mountains from the southwest-northwest-north. Measurements were conducted at the National Centre for Nanoscience and Technology in Beijing (40.00º N, 116.38º E) and the measurement site is located on the roof of the South Building of the National Centre for Nanoscience and Technology (~20 m above ground level) mostly surrounded by smaller buildings. The exception is an 18-floor building approximately 30 m to the north, which may interfere with and even block the wind from this direction. The northern part of the fourth ring highway is situated about 200 m south of the site. However, buildings between the highway and the site reduce the influence from local highway traffic. This location is not affected by major emissions from industries.

The measurements took place from late September to mid-December, 2017, conducted by an extractive electrospray ionisation long-time-of-flight mass spectrometer (EESI L-TOF MS) and a long-time-of-flight aerosol mass spectrometer (L-TOF AMS). A scanning mobility particle sizer (SMPS), consisting of a model 3080 DMA and model 3022 CPC (TSI, Inc., Shoreview, MN, USA), an aethalometer (model AE33, Magee Scientific, Ljubljana, Slovenia) and an Xact 625i Ambient Metals Monitor (Cooper Environmental Services LLC, Tigard, Oregon, USA) were additionally deployed at the site to measure the particle size distribution from 15.7 to 850.5 nm, the equivalent black carbon (eBC) concentration and the mass of 35 different elements in PM_{10} and $PM_{2.5}$, respectively. Ambient air was sampled through a $PM_{2.5}$ cyclone (~ 50 cm above the roof of the measurement site building) at a flow rate of 5 L min^{-1} to remove coarse particles. The air passed through a stainless steel (~ 6 mm outer diameter and ~ 4 mm inner diameter) tube into the EESI L-TOF MS, L-TOF AMS, and SMPS, installed on the same line and in close proximity. Here we focus on OA measurements from late October to mid-December 2017, during which period both the AMS and EESI-TOF were operational.

2.2 Instrumentation

2.2.1 Extractive electrospray ionisation long time-of-flight mass spectrometer (EESI-TOF)

The EESI-TOF provides online, highly time-resolved measurements of the organic aerosol molecular ions without thermal decomposition or ionisation-induced fragmentation. A detailed description can be found elsewhere (Lopez-Hilfiker et al., 2019). The system used in this campaign consists of a recently developed EESI source integrated with a commercial long-time-of-flight (L-TOF) mass spectrometer (Tofwerk AG, Thun, Switzerland), which in this campaign achieved mass resolution of ~8000 Th Th^{-1} at mass to charge ratios *m/z* higher than 170. The EESI-TOF continuously sampled at ~0.8 L min^{-1}, alternating between direct ambient sampling (15 min) and sampling through a particle filter (5 min) to obtain a measurement of the instrument background. The ambient spectrum (M_{total}) minus the average of the immediately adjacent background spectra (before and after) (M_{filter}) yields a difference spectrum, which is taken as the ambient aerosol composition (M_{diff}).

In both modes, the sampled air passes through a multi-channel extruded carbon denuder (with diameter of 4 mm and length of 3 to 4 cm) positioned at 9 cm away from the inlet capillary (see Text S1) which eliminates negative artefacts from semi-volatile species desorbing from the particle filter and positive artefacts when the particle filter acts as a sink of semi-volatile species. The denuder also improves detection limits by reducing the gas-phase background. After sampling for 24 hrs, the denuder was replaced, and regenerated for 24 hrs in an oven at ~200 °C. After the denuder, particles intersect a spray of charged droplets generated by a conventional electrospray probe and the soluble fraction is extracted into the solvent. The droplets then pass through a heated stainless-steel capillary (~250 ◦C), wherein the electrospray solvent evaporates and ions are ejected into the mass spectrometer. Due to the short residence time (~1 ms) in the capillary, the effective temperature experienced by the droplets is much lower than 250 ◦C and no thermal decomposition is observed. Finally, the ions are analysed by a portable high resolution long-time-of-flight mass spectrometer with an atmospheric pressure interface (Junninen et al., 2010). In this campaign, the electrospray consisted of a 1:1 water/acetonitrile mixture doped with 100 ppm NaI, and the mass spectrometer was configured to detect positive ions. Ions are detected in the form of $[M]Na^+$ (where M is the analyte) and other ionisation pathways are mostly suppressed, yielding a linear response to mass (without significant matrix effects) and simplifying spectral interpretation (Lopez-Hilfiker et al., 2019).

The high pollution levels experienced during this campaign presented several operational and analytical challenges for the EESI-TOF, specifically: (1) denuder breakthrough, which increased background signal, led to the detection of spurious signals in the particle phase, and increased the time required to achieve a stable signal following a filter switch between M_{total} and M_{filter}; (2) prevalence of large particles during haze events; and (3) increase in the required frequency of cleaning (unclogging) and realigning the electrospray capillary. These issues and corresponding solutions are discussed in detail in the supplement, and briefly summarised here:

> (1) increased background signals induced by denuder breakthrough compromised high-resolution peak fitting of the spectral region containing particle-phase signals in Tofware (Tofwerk AG, Thun, Switzerland). Therefore, a custom peak fitting algorithm (outside of Tofware) was used, as described in the supplement (see Text S2, Fig. S5 and Fig. S6). Further, denuder breakthrough made it non-trivial to determine whether ions with significantly non-zero difference signal (M_{diff}) derive from the particle phase, gas phase, or desorption from dirtier-than-normal walls (in addition to the standard challenge of background ions with high signal from minor contaminants in the working solution). As only particle-phase ions are desired for further analysis, three criteria were applied for their selection, namely 1) the ratio of signal to uncertainties, 2) ratio of signal to background and 3) estimated saturation vapour mass concentration (C_0) (see Text S3). In addition, the time required to achieve a stable signal following a filter switch between M_{total} and M_{filter} was longer than normal, only the stabilised part of the time series was used for further analysis. Note that compared to normal operation, denuder breakthrough and high background signals significantly increase uncertainties of EESI-TOF data, which poses great challenges in source apportionment and thus motivates the source apportionment strategy in Sect 2.3. Further, the selection of ions in particle phase using saturation vapour mass concentration also introduces a bias against less oxygenated and lower molecular weight species, as well as small organic acids (e.g., small multifunctional acids).
>
> (2) prevalence of large particles during haze events was observed. To prevent the massive sampling losses of large particles, the denuder was pulled back, located at 9 cm away from the inlet capillary (see Text S1).
>
> (3) due to high pollution levels, the clogging of capillary was required more frequently, therefore, the frequency of cleaning (unclogging) and realigning the electrospray capillary increased, which resulted in changes in EESI-TOF sensitivity that uniformly affect all measured ions. Therefore, a normalisation of time-dependent EESI-TOF sensitivity was implemented based on a comparison of $[NaNO_3]Na^+$ measured by the EESI-TOF with nitrate measured by the AMS (see Text S4).

The EESI-TOF achieved ~ 90 % data coverage during the sampling period and all ions were detected as adducts with Na^+. Before high-resolution peak fitting, data were averaged to 2 min. Then the custom peak fitting algorithm (Text S2) was implemented, resulting in 2824 identified ions in total ranging from *m/z* 64 to *m/z* 400. As discussed above, denuder breakthrough yielded stabilisation times from several seconds to several minutes, depending on the ion. Therefore, only the stabilised part of the averaged time series was used for further analysis, corresponding to the last 4 min in the 15 min period of ambient sampling, and the last 2 min in the 5 min filter sampling period, while the remaining time is classified as a transitional period and discarded from further analysis. Adjacent periods of filter sampling were linearly interpolated to obtain an estimated M_{filter} corresponding to each M_{total}; the difference of M_{total} minus the interpolated M_{filter} yields the M_{diff} reported here. To facilitate comparison with bulk mass measurements, EESI-TOF signals were converted from counts per second (cps) to the mass flux of ions to the microchannel plate detector (ag s^{-1}), as follows:

$$M_x = I_x \times (\mathrm{MW}_x - \mathrm{MW}_{CC}) \qquad (1)$$

where M_x and I_x are respectively the mass flux of ions in attograms per second and the ion flux (counts per second, cps) reaching the detector for a given ion of identity x . MW_x and MW_{CC} represent the molecular weight of the ion and the charge carrier (e.g., Na^+), respectively (Lopez-Hilfiker et al., 2019; Qi et al., 2019; Stefenelli et al., 2019). This measured mass flux can in principle be converted to ambient concentration by the instrument flow rate, EESI collection efficiency (the probability that the analyte-laden droplet enters the inlet capillary), EESI extraction efficiency (the probability that a molecule dissolves in the spray), ionisation efficiency (the probability that an ion forms and survives declustering forces induced by evaporation and electric fields), and ion transmission efficiency (the probability that a generated ion is transmitted to the detector). However, since several of these parameters are compound-dependent and remain uncharacterised, mass concentration at this stage cannot be determined (Lopez-Hilfiker et al., 2019).

After application of the criteria in Text S3, 401 ions are retained for further analysis. As will be discussed in Sect. 2.3, source apportionment was conducted on the EESI-TOF data by positive matrix factorisation (PMF), which requires as inputs the mass spectral time series and corresponding uncertainties. The input data matrix $M_{diff}(i,j)$ is calculated according to Eq. (2):

$$M_{diff}(i.j) = \mathrm{M}_{total}(i,j) - M_{filter,estimate}(i,j) \qquad (2)$$

where $M_{total}(i,j)$ denotes the signal of spectra measured in total sampling period, $M_{filter,estimate}(i,j)$ denotes signal of estimated background spectra after interpolation of the filter sampling period, and $M_{diff}(i,j)$ denotes signal of the difference spectra between total sampling period and estimated background and consists of 401 (ions) × 1239 (time points). The error matrix corresponding to M_{diff} is estimated by adding in quadrature the uncertainty of total sampling measurement $\sigma_{total}(i,j)$ and filter sampling measurement $\sigma_{filter,estimate}(i,j)$, which are in turn based on ion counting statistics and detector variability (Allan et al., 2003b), shown in Eq. (3):

$$\sigma_{diff}(i,j) = \sqrt{\sigma^2_{total}(i,j) + \sigma^2_{filter,estimate}(i,j)} \qquad (3)$$

2.2.2 Long time-of-flight aerosol mass spectrometer (L-TOF AMS)

A long time-of-flight aerosol mass spectrometer (L-TOF AMS, Aerodyne Research Inc.) equipped with a $PM_{2.5}$ aerodynamic lens was deployed to monitor the non-refractory (NR) particle composition with a time resolution of 2 min. The instrument is described in detail elsewhere (Canagaratna et al., 2007). Briefly, particles are sampled continuously at ~0.1 L min^{-1} into a 100 µm critical orifice and then a $PM_{2.5}$ aerodynamic lens, which focuses the particles into a narrow beam and accelerates them to a velocity inversely related to their vacuum aerodynamic diameter (Williams et al., 2013). The particle beam impacts on a heated tungsten surface (standard AMS vaporiser, ~ 600 ℃, and ~ 10^{-7} Torr) and the NR components flash vaporise. The resulting gases are ionised by electron ionisation (EI, ~ 70 eV) and measured by a TOF mass spectrometer. The instrument was calibrated for ionisation efficiency (IE) at the beginning, middle, and end of the campaign by a mass-based method using 350 nm NH_4NO_3 particles. To eliminate the influence from relative humidity (RH) on collection efficiency (CE), a Polytube Dryer Gas Sample Dryer (Perma Pure LLC) was mounted in front of the AMS inlet. A composition-dependent collection efficiency (CDCE) was applied to correct the measured aerosol mass (Middlebrook et al., 2012), and no size-dependent CE corrections were applied. Data analysis was performed in Igor Pro 6.39 (Wavemetrics, Inc.) using SQUIRREL 1.57 and PIKA 1.16 ((Donna Sueper, ToF-AMS high-resolution analysis software).

In conventional AMS data analysis, the signal from CO^+ cannot be directly determined due to interference from N_2^+, and is instead assumed to be equal to that of CO_2^+. However, the increased mass resolution provided by the L-TOF detector was sufficient in this study to allow direct peak fitting of CO^+, which is reported herein. As shown by Pieber et al. (2016), CO_2^+ signal in the AMS derives not only from OA and gaseous CO_2, but is also generated directly from the vaporiser in the presence of some inorganic aerosols, notably NH_4NO_3. This effect was corrected using 350 nm NH_4NO_3 aerosol according to the method recommended by Pieber et al. (2016) and the nitrate fraction was not high enough to require the composition-dependent method of Freney et al. (2019). The CO_2^+ signal resulting from nitrate was found to be 4.4 % of the total CO_2^+ signal. In principle, spurious CO^+ signal can be generated by the same process, either through fragmentation of CO_2 or directly via related oxidation reactions. However, the CO^+ signal was below detection limit for the NH_4NO_3 test aerosol. We therefore assumed a value of 0.4 % of total CO^+ signal, which corresponds to 10 % of CO_2^+ as given by the 70 eV EI reference mass spectrum of CO_2 according to the NIST Standard Reference Simulation Website (Shen et al., 2017).

Source apportionment (see Sect. 2.3) was performed on the AMS OA data and requires as inputs the OA mass spectral time series and corresponding uncertainties. The data matrix was constructed by including both (1) ions with known molecular formula for $m/z \leq 120$ and (2) the integrated signal across each integer m/z for m/z 121 to m/z 300. This allows inclusion of chemical information at m/z where the number of possible ions and AMS resolution are insufficient for robust identification and quantification of individual ions. Of particular note for the current dataset, inclusion of the high m/z data allows inclusion of polycyclic aromatic hydrocarbons (PAHs) in the PMF analysis. Uncertainties were calculated according to the method of Allan et al. (2003a), and account for electronic noise, ion-to-ion variability at the detector, and ion counting statistics, with a minimum error enforced according to the method of Ulbrich et al. (2009). As recommended by Paatero and Hopke (2003), variables with weak SNR ($0.2<SNR<2$) were down-weighted by a factor of 2 and variable with low SNR ($SNR<0.2$) were removed from the input matrices.

Ions that were not independently fit but calculated as a constant ratio of CO_2^+, i.e., O^+, HO^+ and H_2O^+, were removed from PMF analysis to avoid overweighting the contribution of CO_2^+. After obtaining the PMF solutions, the contribution of these ions was recalculated and reinserted into the factor profile. The resulting factor profiles were re-normalised, likewise the total mass. Note that although typical AMS source apportionment studies likewise remove CO^+, the increased mass resolution of the L-TOF detector allows an independent measurement of CO^+ and this ion is therefore retained for PMF. Isotopes were removed prior to PMF analysis (to avoid overweighting the parent ions) and reinserted afterwards.

2.3 Source Apportionment Technique

Source apportionment was performed using the positive matrix factorisation (PMF) model, implemented within the multilinear engine (ME-2). AMS and EESI-TOF measurements are highly complementary, with the AMS providing robust quantification but limited chemical resolution, and the EESI-TOF providing a linear but hard-to-quantify response with high chemical resolution. As a result, integrating these two instruments in single source apportionment model represents a promising strategy for improved source apportionment, especially of the SOA fraction. Conceptually, this can be executed in three ways: (1) PMF analysis on a single dataset containing both AMS and EESI-TOF data; (2) PMF analysis of EESI-TOF-only data to identify factors and determine their time series, followed by PMF on AMS-only data with factor time series constrained according to EESI-TOF results; or (3) PMF on AMS-only data to determine factor time series, followed by PMF on EESI-TOF-only data with constrained factor time series to facilitate chemical interpretation of the AMS-determined factors. For the present analysis, we selected method (3) because of EESI-TOF data quality issues related to denuder breakthrough (see Sect. 2.2.1) and the appearance of several interesting-but-unexplained factors in preliminary AMS PMF analysis.

For the AMS PMF analysis, one factor related to traffic and one factor related to cooking activities were constrained using the *a* value approach for the HOA spectra from Mohr et al. (2012) and the COA spectra from Crippa et al. (2013). Based on the result from PMF analysis on AMS data, PMF was then performed for the EESI-TOF dataset, by constraining all factor time series retrieved from the AMS PMF source apportionment, except for the HOA time series (which was excluded because the hydrocarbon-like species dominating HOA are undetectable by the EESI-TOF extraction/ionisation scheme used here). This is conceptually similar to chemical mass balance (CMB), except that here the factor time series are constrained instead of factor profiles. This allows AMS-resolved factors, notably those related to SOA, to be described in terms of the higher chemical resolution achievable by the EESI-TOF. To explore the robustness and uncertainties of each step in our integrated source apportionment, bootstrap analysis was conducted individually on the AMS PMF solution and the second step "CMB-analogue" result from the EESI-TOF.

Note that this strategy would not necessarily be the optimal use of co-located AMS and EESI-TOF data, if both instruments were performing optimally. In particular, it neglects to take advantage of the higher chemical resolution of the EESI-TOF for factor separation. However, for the specific situation encountered in this study, where (1) interpretation of the standalone EESI-TOF data is significantly complicated by denuder breakthrough; (2) high EESI-TOF backgrounds may increase the uncertainty of peak fitting; and (3) AMS PMF resolves multiple factors that are temporally distinct but difficult to interpret chemically, we believe the selected approach maximises the explanatory power of the dataset. As an alternative strategy, a preliminary PMF of standalone EESI-TOF data was attempted, but did not yield interpretable results. This is likely because the PMF model, as will be discussed in the next section, requires detector linearity and static factor composition. Denuder breakthrough compromises both assumptions, because the volatile and semi-volatile contributions to factor profiles depends on the time-dependent state of the denuder (Brown et al., 2021). The EESI-TOF data processing protocols utilised above reduce but do not eliminate this issue. However, by constraining the EESI-TOF PMF solution with AMS factor profiles, the solution becomes weighted towards explaining temporal trends observed in the particle phase. Further, by utilising the EESI-TOF for qualitative (factor identification) rather than quantitative (factor resolution) purposes, the impact of artifacts introduced by gaseous signals is minimised.

Determination of the proper number of factors to obtain the most interpretable PMF solution is partly subjective. In this paper, criteria to identify and interpret the factors implemented include comparison of correlation between factor time series or profiles with external references, and to investigate the factor's distinctive chemical signatures.

2.3.1 Positive matrix factorisation (PMF)

Positive matrix factorisation (PMF) was implemented using the Multilinear Engine (ME-2) (Paatero, 1997), with model configuration and post-analysis performed with the Source Finder interface (SoFi, version 6.8b) (Canonaco et al., 2013), programmed in Igor Pro 6.39 (Wavemetrics, Inc.). PMF is a bilinear receptor model which describes the input data matrix (here the mass spectral time series) as a linear combination of static factor profiles (in this case characteristic mass spectra, representing specific sources or/and atmospheric processes) and their corresponding time-dependent source contributions, as described in Eq. (4):

$$\mathbf{X} = \mathbf{G} \times \mathbf{F} + \mathbf{E} \qquad (4)$$

Here **X** is the input data matrix with dimensions of $m \times n$, representing m measurements of n variables (here ions or *m/z*), **G** and **F** are respectively the static factor time series with the dimension of $m \times p$, and factor profiles with the dimension of $p \times n$, where p is the number of factors in the PMF solution, and is determined by the user. **E** is the residual matrix. **G** and **F** in Eq. (4) are solved by a least-squares algorithm that iteratively minimises the quantity Q, which is defined in Eq. (5) as the sum of the squares of the uncertainty-weighted residuals:

$$Q = \sum_i \sum_j \left(\frac{e_{ij}}{\sigma_{ij}} \right)^2 \qquad (5)$$

Here e_{ij} is an element in the residual matrix **E**, and σ_{ij} is the corresponding element in the measurement uncertainty matrix, where i and j are the indices representing measurement time and ion (or integer *m/z*), respectively.

PMF is subject to rotational ambiguity, in that different combinations of the **G** and **F** matrices may yield solutions with the same or similar Q. In practice, this often leads to mixed or unresolvable factors. Here we explore a subset of the possible PMF solutions, directed towards environmentally meaningful rotations. This is achieved via the a-value approach, wherein one or more factor profiles and/or factor time series are constrained using reference factors profiles or/and time series, with the scalar a ($0 \leq a \leq 1$) determining the tightness of constraint. This approach has been shown to improve solution quality relative to unconstrained PMF (Crippa et al., 2014; Canonaco et al., 2013). The a-value approach determines the extent to which the resolved factor profiles $\left(g_{i,k}\right)_{solution}$ and time series $\left(f_{k,j}\right)_{solution}$ may differ from the input values ($g_{i,k}$ or $f_{k,j}$), as shown in Eq. (6a) and Eq. (6b):

$$\left(g_{i,k}\right)_{solution} = g_{i,k} \pm a \times g_{i,k} \qquad (6a)$$

$$\left(f_{k,j}\right)_{solution} = f_{k,j} \pm a \times f_{k,j} \qquad (6b)$$

Note that the final value of $\left(g_{i,k}\right)_{solution}$ and $\left(f_{k,j}\right)_{solution}$ may slightly exceed the prescribed limits due to post-PMF renormalisation of the **G** and **F** matrices. Here the a-value approach was used for both the AMS and EESI-TOF datasets. Sensitivity tests to determine an appropriate range of a-values were performed in combination with bootstrap analysis, as described in the following section.

2.3.2 Bootstrap Analysis

Bootstrap analysis (Davison and Hinkley, 1997) was performed to characterise solution stability and estimate uncertainties. Bootstrapping creates a set of new input and error matrices by random resampling of rows from the original input data and error matrices. This resampling preserves the original dimensions of the input datamatrix, but randomly duplicates some time points while excluding others (Paatero et al., 2014). For the AMS dataset, we performed 1000 bootstrap runs on an eight-factor solution, with HOA and COA factors constrained. For each factor, a random a-value was selected for each bootstrap run, ranging from 0 to 0.5 with a step size of 0.1. For the EESI-TOF dataset, 1000 bootstrap runs were performed on a 7-factor solution. Each EESI-TOF factor was constrained by a factor from the AMS 8-factor solution, with AMS HOA excluded because it is not detectable in the EESI-TOF due to low solubility and ionisation efficiency. For the EESI-TOF bootstrapping, each factor was constrained with a randomly selected a-value ranging from 0 to 0.6 with a step size of 0.1.

Conceptually, each bootstrap solution can be classified in three ways: (1) qualitatively similar to the base case; (2) qualitatively similar to the base case, but with 2 or more factors mixed; (3) fundamentally different from the base case, e.g., one or more factors has appeared and/or disappeared. For characterising uncertainties in the factor profiles and/or time series, only solutions of type (1) are considered. We therefore use the solution classification methods of Stefenelli et al. (2019), which are based on determining whether each factor profile and/or time series from the base case is with statistical significance more similar to one and only one factor in a given bootstrapped solution. This method is implemented in three steps: 1) creation of a base case, 2) calculation of the Spearman correlation between the time series of each factor from the base case vs. each factor from the bootstrap solution, 3) sorting the resulting correlation matrix such that the highest correlation coefficients fall on the diagonal, 4) each correlation coefficient on the diagonal is compared to values on the row and column to evaluate whether this coefficient is statistically significant higher than other values on the same row or column, by *t*-test analysis. The bootstrap solutions that fail to meet this criterion are classified as “mixed”.

The definition of a mixed solution therefore depends on the selected confidence level p, which is evaluated here by a sensitivity test of p ranging from 0.05 to 0.95 with a step of 0.05; the number of solutions classified as “mixed” rises as p increases (Fig. S7). This enables identification of the solutions most likely to be classified as “mixed” for each increment of p. These solutions are manually inspected to confirm that they do in fact appear mixed, and the final p is selected once this no longer holds true. Using this method, a final p of 0.40 for AMS was chosen, yielding 918 accepted bootstrap runs. For EESI-TOF bootstrap analysis, since the time series of all factors are constrained, all runs are considered as good runs and utilised to explore the variability of factor profiles.

2.3.3 z-score analysis of factor profiles

The dynamic range of EESI-TOF and AMS ion signal concentrations spans several orders of magnitude. Key chemical information may be contained in low-intensity ions, which are not readily evident from the factor profile. To assist in identifying such spectral features, we calculate the z-score of each ion across the factor profile matrix as follows:

$$z_{p,g} = (x_{p,g} - \mu_p)/\sigma_p \qquad (7)$$

Here $z_{p,g}$ and $x_{p,g}$ are the z-score and the relative intensity of ion p in factor profile g, respectively, and μ_p and σ_p is the mean and standard deviation of relative intensity of ion p in all PMF factors. The z-score is a signed, dimensionless quantity whose absolute value is to describe the distance between an observation x and population mean μ in the unit of standard deviation σ (Larsen and Marx, 2018). It therefore highlights ions whose contribution to a factor profile is unexpectedly high (or low), independent of absolute signal magnitude. In this study, z-score is used to identify key ions that are unique to a specific factor or small subset of factors, as will be discussed in Sect. 3.3.

3. Results

3.1 Campaign overview

Figure 1 shows an overview of the NR-$PM_{2.5}$ composition and meteorological parameters observed during the campaign. During the measurement period, we observed nine haze episodes, classified as light haze (NR-PM2.5 concentrations from 20 to 150 µg m^{-3}) or severe haze (NR-$PM_{2.5}$ concentrations above 150 µg m^{-3}). Of these, four haze episodes occurred during the non-heating season, four during the heating season, and one episode bridged the transition date. Consistent with previous studies (Duan et al., 2020; Duan et al., 2019; Zhao et al., 2019; Xu et al., 2019; Sun et al., 2016a; Sun et al., 2016b), alternating haze episodes and clean periods corresponded systematically to changing meteorological conditions. Haze build-up was associated with stagnant air masses with slow wind speed (< 1.5 m s^{-1}) mainly from the south or southwest, and terminated by air masses with high wind speed (> 3.0 m s^{-1}) from the north or northwest (Fig. 1b and 1c). Different from previous studies in Beijing in 2014 and 2015, where haze events lasting more than five days were observed (Zhao et al., 2019; Xu et al., 2019; Sun et al., 2016b), all haze events in this campaign lasted for two to four days. The maximum concentration of NR-$PM_{2.5}$ measured by the L-TOF AMS exceeded 100 µg m^{-3} in only one haze event (4 to 7 November), and the mean NR-$PM_{2.5}$ concentration in the haze episodes was 36.6 ± 22.7 µg m^{-3}, which is even lower than mean concentrations of NR-PM_1 observed in Beijing winter from 2013 (89.3 ± 85.6 µg m^{-3}) to 2016 (64 ± 59 µg m^{-3}) (Zhao et al., 2019; Xu et al., 2019; Sun et al., 2016a; Zhang et al., 2014).

Aerosol bulk composition differs between the non-heating and heating seasons, indicating changes in sources and/or chemical processes. Organic aerosol (OA) is the major fraction of NR-$PM_{2.5}$ throughout the campaign period, with a mean contribution of 54.0 %, consistent with previous winter studies in Beijing (Zhao et al., 2019; Xu et al., 2019; Elser et al., 2016). The temporal evolution of OA shows that the contribution in haze episodes increased from 41.0 % during the non-heating season to 54.0 % during the heating season. This contrasts with nitrate, which is the second largest contributor to NR-$PM_{2.5}$ in this study and contributes 37.0 % of NR-$PM_{2.5}$ in non-heating season haze events but decreases to 23.0 % during heating season haze events. Of particular note is the non-heating season haze event from 4 to 7 November, where nitrate comprises more than 50.0 % of NR-$PM_{2.5}$, exceeding OA contribution to total mass in this event. This event is discussed in detail in Sect. 3.3.4 and Sect. 4. It is also worth noticing that the nitrate concentration and its contribution was lower than sulphate during every clean period, but higher during every haze episode. The mean nitrate/sulphate ratio in the present study is 2.8±2.4, a significant increase compared to observations in 2014 (0.7±0.6) and 2016 (1.4±0.9) from Xu et al. (2019). In addition, the nitrate/sulphate ratio exceeded 1 for 63 % of measurements in the present study, compared with only 24 % in 2014. It is clear that the contribution of nitrate in haze events gradually exceeded the contribution of sulphate from 2014 to 2017, indicating nitrate is playing an increasingly important role relative to sulphate in haze formation, mainly due to large reduction in SO_2 emissions from coal fired power plants in Beijing and surrounding areas.

3.2 AMS source apportionment

With the combination of HR ions (range from *m/z* 12 to *m/z* 120, see Table S2) and UMR sticks (from *m/z* 121 to *m/z* 300) in the PMF input matrix, eight factors were resolved, including four primary and four secondary organic factors. Figure 2 shows the averaged MS profiles of the selected eight-factor solution and corresponding relative contribution of each ion (i.e., fraction of signal from a given ion apportioned to each factor), while Fig. 3 shows the factor time series in terms of both absolute concentration and OA mass fraction. Diurnal patterns are shown in Fig. 3c. The four POA factors consist of a traffic related factor (hydrocarbon-like OA, HOA), cooking-related OA (COA), and two solid fuel combustion-related factors (biomass burning OA, BBOA, and coal combustion OA, CCOA). The four primary factors retrieved in this solution (HOA, COA, BBOA, and CCOA) have been resolved in several previous winter studies in Beijing (Huang et al., 2014; Elser et al., 2016; Hu et al., 2016; Sun et al., 2016a). However, the SOA factor resolution is unusual. AMS source apportionment studies typically report one or two oxygenated organic aerosol (OOA) factors attributed to SOA that are distinguished by the extent of oxygenation, which is in turn typically linked to volatility, age, or season. Here, we report four secondary factors, consisting of two more-oxygenated OOAs (MO-OOAs) and two less-oxygenated OOAs (LO-OOAs). For reasons described below and in Sect. 3.3, the one MO-OOA factor is attributed to aqueous phase chemistry (MO-OOA_{aq}) and the other to solid fuel combustion (MO-OOA_{SFC}), while one LO-OOA factor is attributed to solid fuel combustion (LO-OOA_{SFC}), and the other considered a non-source-specific factor denoted as (LO-OOA_{ns}).

In selecting the PMF solution that best represents the AMS dataset, we considered both mathematical diagnostics (e.g., Q/Q_{exp}) and the interpretability of the retrieved factors. Evaluation of factor interpretability includes: 1) correlation of the time series with external data, 2) comparison of factor diurnal cycles with known source activity and previous measurements in Beijing; 3) identification of source-specific spectral features; and 4) differences in factor trends between heating/non-heating and/or haze/non-haze periods. Solutions from five to ten factors were explored (Fig. S9 to Fig. S14), with an eight-factor solution selected as the best representation of the data according to the above criteria. Solutions with less than six factors showed evidence of mixed primary sources. The seven- and eight-factor solutions resolve additional OOA factors, which have clear temporal and compositional differences that support their separation and interpretation. Higher-order solutions lead to uninterpretable splitting of OOA factors. Therefore, the eight-factor solution is retained for further analysis.

HOA -- The HOA spectrum (Fig. 2a) is characterised by alkyl fragments, especially $C_nH_{2n-1}^+$ and $C_nH_{2n+1}^+$. Major ions include $C_3H_7^+$, $C_4H_9^+$, $C_5H_{11}^+$ (Zhao et al., 2019; Xu et al., 2019; Sun et al., 2016a; Elser et al., 2016; Zhang et al., 2014; Ng et al., 2011). It also shows good correlation with CO and eBC (r^2 = 0.50 and 0.70, Fig. S16), which are tracers for traffic emissions (Sun et al., 2016a; Zhang et al., 2014; Chan et al., 2011). Concentrations of this factor are elevated overnight due to boundary layer dynamics, and exhibit peaks from 06:00 to 09:00 and from 17:00 to 21:00, corresponding respectively to the morning and evening rush hours (Fig. 3c and Fig. S15). The averaged concentration during the evening peak (0.5 μg m^{-3}) is almost twice as high as the morning peak (~0.3 μg m^{-3}), due to the low planetary boundary layer height and resulting accumulation of vehicle emissions at night (Sun et al., 2016a; Han et al., 2009). This diurnal pattern is consistent with other winter studies in Beijing (Sun et al., 2016a; Zhang et al., 2014). However, the averaged relative contribution of HOA factor to total mass (~3.0 %) is significantly lower than previous studies (~10.0 %) (Elser et al., 2016; Hu et al., 2016; Sun et al., 2016a; Zhang et al., 2014; Huang et al., 2010), this indicates that primary traffic emissions comprise a minor fraction of OA during both non-heating and heating periods.

COA -- The COA spectrum contains both alkyl fragments and slightly oxygenated ions, consistent with aliphatic acids from cooking oils (Hu et al., 2016). It is typically characterised by a ratio of $C_3H_3O^+$ to $C_3H_5O^+$ which greater than 2.0, and is 3.4 in this study (Xu et al., 2019; Zhao et al., 2019; Sun et al., 2016a; Sun et al., 2016b; Crippa et al., 2013; Mohr et al., 2012). The time series of the COA factor strongly correlates with AMS $C_6H_{10}O^+$ (*m/z* 98), a good tracer for cooking activities reported by many studies (Xu et al., 2019; Zhao et al., 2019; Elser et al., 2016; Hu et al., 2016; Sun et al., 2016a; Sun et al., 2016b; Mohr et al., 2012; Sun et al., 2011), with r^2 = 0.96 and 60.1 % of the mass of this ion being apportioned to COA. The diurnal cycle shows three peaks: from 07:00 to 09:00 at breakfast and from 12:00 to 13:00 at lunch time and a larger peak from 18:00 to 21:00 during dinner (Fig. 3c and Fig. S15). This three-peak diurnal pattern agrees with the diurnal cycle observed by Sun et al. (2016a), but differs from many other studies at different sites during winter in Beijing, where only two peaks are evident and the morning peak from 07:00 to 09:00 is missing. This suggests a dependence on the proximity to local emissions (Xu et al., 2019; Elser et al., 2016; Hu et al., 2016; Zhang et al., 2014). The ratio of dinner peak to lunch peak is about 2.0, similar to the values of ~2.0 and 2.3 observed by Elser et al. (2016) and Hu et al. (2016), respectively, whereas Sun et al. (2016a) reports a ratio of 1.29. Overall, the COA factor is a non-negligible contributor to total OA, with a relative contribution of 6 %, lower than 18 % in 2013 (Sun et al., 2016a), 25 % in 2014 and 16 % in 2016 wintertime (Xu et al., 2019). The mean concentration is 0.3 μg m^{-3}, lower than previous studies (Xu et al., 2019; Zhao et al., 2019; Elser et al., 2016; Hu et al., 2016; Sun et al., 2016a; Sun et al., 2016b; Mohr et al., 2012; Sun et al., 2011).

BBOA – Consistent with other studies in Beijing (Zhao et al., 2019; Elser et al., 2016; Hu et al., 2016; Sun et al., 2016a), a BBOA factor was resolved. Typically, the BBOA factor mass spectrum is characterised by increased contributions from $C_2H_4O_2^+$ at *m/z* 60 and $C_3H_5O_2^+$ at m/z at 73, which is typical of anhydrosugars such as levoglucosan (Alfarra et al., 2007; Lanz et al., 2007; Sun et al., 2011). However, although the contribution of the BBOA factor to $C_2H_4O_2^+$ is the highest (28.6 %) among those factors and its correlation is also high, with r^2 = 0.62, other primary sources like CCOA and COA also contribute significant fractions of $C_2H_4O_2^+$ signal. BBOA also correlates strongly with $C_3H_5O_2^+$ (r^2 = 0.71) and $C_6H_6O_2^+$ (r^2 = 0.81), which are also typical of biomass burning activities (Lanz et al., 2007; Sun et al., 2011). The O:C ratio and N:C ratio of this factor is 0.4 and 0.02, respectively, agreeing quite well with the values found in other studies (Xu et al., 2019; Zhao et al., 2019; Hu et al., 2016).

The BBOA time series is event-driven, with both concentrations and relative contributions increasing during haze events, especially the haze event from 18 to 22 November (68.7 % of total OA). Apart from this event, the BBOA concentration increase during other haze events is also clear, regardless of non-heating vs. heating season. Overall, the average BBOA concentration for the haze events was 1.9 µg m^{-3}, with a maximum of 19.1 µg m^{-3} for the event from 18 to 22 November, and ~0.1 µg m^{-3} for the clean periods, both lower than the study in mid-winter from 2013 to 2014 (Sun et al., 2016a) and the studies covering the same time period of the early winter in 2014 and 2016 (Xu et al., 2019). Its relative contribution to total OA is 15.4 % for haze periods and 8.2 % for the clean period, respectively, consistent to observations of Elser et al. (2016), who report 13.9 % and 8.9 % for haze and clean periods in wintertime in Beijing, respectively.

CCOA – apart from alkyl fragments $C_nH_{2n-1}^+$ and $C_nH_{2n+1}^+$, the main feature of the CCOA profile is the high contribution from PAHs (approximately *m/z* 175 to 300), especially in the high *m/z* range, consistent with studies from Elser et al. (2016), Zhang et al. (2008) and Xu et al. (2006). In the high mass range, PAHs contribute an increasingly higher fraction at higher *m/z* (Fig. 2b). A series of strong signals are found in the factor profile at *m/z* 115 ($C_9H_7^+$), 128, 139, 152, 165, 178, 189, 202, 215, 226, 239 and 252, which have been shown to be characteristic of aromatics and PAHs (Dzepina et al., 2007). Moreover, the time series of this factor and these signatures correlate quite well with r^2 of 0.81 ($C_9H_7^+$), 0.80 (*m/z* 128), 0.83 (*m/z* 139), 0.90 (*m/z* 152), 0.90 (*m/z* 165), 0.93 (*m/z* 178), 0.94 (*m/z* 189), 0.97 (*m/z* 202), 0.97 (*m/z* 215), 0.98 (*m/z* 226), 0.96 (*m/z* 239) and 0.98 (*m/z* 252), respectively, consistent with observations from Dzepina et al. (2007), Hu et al. (2013), Hu et al. (2016) and Sun et al. (2016a).

Coal is used widely for domestic heating in northern China including the greater Beijing area and surrounding provinces (Zhang et al., 2008), but is not permitted for residential use in the downtown area. Instead, beginning on 15 November, power plants using natural gas provide heating to every household in the Beijing downtown area, and municipal coal combustion begins to provide heating to the surrounding area. Interestingly, the time series of the CCOA factor reflects this seasonal transition, as the mean daily maximum concentration increased from 2.9 µg m^{-3} before 15 November to 5.9 µg m^{-3} after. Similar to other studies (Elser et al., 2016; Hu et al., 2016; Sun et al., 2016a; Zhang et al., 2014), the diurnal concentration peaks at night between 21:00 and 06:00 with an average contribution of 15.5 % to total OA, and decreases during the day from 07:00 to 20:00 with an average contribution of 7.4 %, consistent with domestic heating (Fig. 3c and Fig. S15). Overall, the mean contribution to total OA is 11.4 %, with 7.1 % in the non-heating period and 14.7 % in the heating season. The latter number agrees with observations conducted in the heating period in Beijing during winter, ranging from 10 % to 30 % (Elser et al., 2016; Hu et al., 2016; Zhang et al., 2014; Sun et al., 2013).

OOAs – As noted above, the OOA factors resolved here differ from previous AMS studies in Beijing, where only one or two OOA factors were resolved and classified based on volatility (semi-volatile OOA and low-volatility OOA) (Zhao et al., 2019; Zhang et al., 2014; Hu et al., 2013) or oxidation state (more-oxygenated OOA and less-oxygenated OOA) (Xu et al., 2019; Elser et al., 2016; Sun et al., 2016a; Sun et al., 2013). In this study, two more-oxygenated OOAs (MO-OOA) and two less-oxygenated OOA (LO-OOA) were resolved. The OOA factors are characterised by higher signal from CO_2^+ than found in the POA factors. In this study, CO_2^+ comprises approximately 15.0 % of the two MO-OOA factors. For the two LO-OOAs, the CO_2^+ contribution to the total signal is only 3.8 % in LO-OOA$_{SFC}$ and 5.4 % in LO-OOA$_{ns}$, while the ratio of CO_2^+ to $C_2H_3O^+$ is still higher than for the POAs. Moreover, a higher contribution of the C_xH_y group is observed in the LO-OOA factors than in the MO-OOA factors. Each OOA factors has a significantly different time series, corresponding to specific haze events and/or seasonal changes, providing a first suggestion that their separation may be meaningful.

Among the MO-OOA factors, one factor (influenced by aqueous phase chemistry, defined as MO-OOA$_{aq}$) has high absolute and relative concentrations during a single haze event from 4 to 7 November (maximum 16.2 µg m^{-3}, > 60.0 % of the total OA mass), but is a minor component throughout the rest of the campaign. In contrast, the other MO-OOA factor (aged solid fuel combustion emissions, defined as MO-OOA$_{SFC}$) is a minor component before 15 November, but both its mass and relative contribution steadily increase during the heating season, especially during haze periods. This is consistent with the temporal pattern of CCOA, suggesting this factor may be linked to coal combustion activities. The temporal evolution of the two LO-OOA factors are also distinguishable. The concentration of one factor (LO-OOA$_{SFC}$) increases in every haze episode under stagnant conditions and is correlated with the total OA time series (r^2 =0.91), whereas the other factor (LO-OOA$_{ns}$) exhibits a clear diurnal pattern in the non-heating season, but this diurnal cycle is absent during the heating season. Interestingly, the contribution of the LO-OOA$_{ns}$ factor to total OA is higher during the clean days, suggesting this factor may be more influenced by regional processes. The chemical characteristics and sources/processes governing these OOA factors are discussed in detail in the next section, in conjunction with the EESI-TOF analysis.

3.3 Investigation of factor composition by EESI-TOF

As discussed in Sect. 2.3, PMF of the EESI-TOF mass spectral time series was conducted on a 7-factor solution where all factor time series were constrained by the seven non-HOA factors retrieved from AMS PMF. The EESI-TOF factor time series are compared to their AMS counterparts in Fig. S17, and scatter plots of EESI-TOF vs AMS on a factor-by-factor basis are shown in Fig. S18. These comparisons suggest that the EESI-TOF factor time series mostly reflect the main trends in the AMS factor time series. This approach enables a more chemically specific interpretation of the retrieved AMS factors, which both supports POA factor identification and provides additional insight into the sources and processes governing SOA. Note that all factors resolved in this study are based on time series derived from AM PMF analysis, therefore, in the following sections, these factors are discussed from the chemical perspective of EESI-TOF and no subscript is added to distinguish factors represented by PMF analysis of AMS or EESI-TOF. The PMF result of the EESI-TOF time series was used as the base case for bootstrap runs, and all the bootstrap runs were retained for further analysis. EESI-TOF factor profiles (corresponding to AMS-derived factor time series) are interpreted by 1) comparison between these factor profiles and mass spectra retrieved from a chamber study using an EESI-TOF (Amelie Bertrand, personal communication) and/or field studies (Qi et al., 2019; Stefenelli et al., 2019), 2) identification of key ions in the factor profiles by z-score analysis introduced in Sect. 2.3.3. The time series and factor profiles of the seven-factor solution are shown in Fig. 4.

We discuss the three primary factors in Sect. 3.3.1 and the four OOA factors individually in the subsequent sections. For better interpretation, we present carbon number distribution plots from the EESI-TOF factor profiles colour-coded by different families in Fig. 5 and Fig. 6 for the three POA factors, and Fig. 7 and Fig. 8 for the four OOA factors respectively. In the carbon number distribution plots, ions are classified first based on carbon numbers (*x*-axis) and ions with same number of carbons are further divided into different categories based on H:C and O:C ratios (colour code). Figure 9 shows Van Krevelen plots (atomic H:C vs. O:C ratio) for the four OOA factors based on AMS factor profiles coloured by number of nitrogen atoms in each fragment, and sized by the median z-score across all bootstrap runs, with large markers denoting ions having z-score > 1.5.

3.3.1 POA factors

COA – Consistent with Qi et al. (2019) and Stefenelli et al. (2019), the mass spectrum of this factor (Fig. 4b) is characterised by having most of the mass at ions with high *m/z*. These ions at high *m/z* are likely long-chain fatty acids or/and alcohols related to cooking emission and oils (Liu et al., 2017b). For example, this factor is characterised by long-chain acids like $C_{18}H_{34}O_2^+$, $C_{19}H_{36}O_2^+$ and $C_{21}H_{38}O_3^+$, which apportion 87.2 %, 76.2 %, and 92.3 % of their total mass to this factor, and they are also unique ions in this factor, with z-scores of 2.61, 2.95 and 3.34, respectively.

BBOA – The mass spectrum of BBOA (Fig. 4b) is characterised by a strong signal at $C_6H_{10}O_5$, corresponding to levoglucosan and its isomers. Levoglucosan is a well-established tracer for primary aerosols formed from pyrolysis of cellulose in biomass burning activities. This ion contributes 6.6 % to the mass in this factor, about 4.5 times higher than the second strongest ion, consistent with previous field and laboratory measurements of biomass burning by the EESI-TOF. Both Qi et al. (2019) (winter measurements in Zurich, Switzerland) and Bertrand (personal communication) (chamber study of wood burning emissions) showed levoglucosan and its isomers to be the dominant ion in EESI-TOF spectra of primary wood burning, with contributions of 13.0 % and 21.0 % respectively. In addition, the ion series $C_{10}H_{14}O_x$ ($x \geq 4$) is observed in the BBOA and aged-SFC factors, consistent with Qi et al. (2019).

CCOA – as shown in the carbon number distribution plots (Fig. 5 and Fig. 6), lower H:C and O:C ratios are observed compared to other factors, especially for species with more than 10 carbons, suggesting increased contributions from aromatic acids. This is consistent with Zhang et al. (2008) who found that particles generated from industrial boilers typically contain a considerable fraction from both aromatic acids and aliphatic acids. Note that PAHs, which comprise the unique AMS spectral marker, are not detectable by the EESI-TOF extraction/ionisation scheme used here.

3.3.2 MO-OOA$_{SFC}$

As noted in Sect. 3.2, the AMS MO-OOA$_{SFC}$ mass spectrum is consistent with OOA factors characteristic of SOA, and represents aged, oxygenated emissions from solid fuel combustion. The carbon number distribution of the EESI-TOF MO-OOA$_{SFC}$ mass spectrum (Fig. 7b) shows several notable features that provide further insight into its source. First, the contribution of $C_xH_yO_z$ ions with low H:C is significantly higher than for the other OOA factors. Specifically, $(C_xH_yO_z)_{H:C\leq1.3}$ comprises 11.6 % of the total signal and 20.9 % of $C_xH_yO_z$; for the other non-SFC related OOA factors, $(C_xH_yO_z)_{H:C\leq1.3}$ comprises a maximum of 8.6 % of the total signal and 10.9 % of $C_xH_yO_z$. The high fraction from low H:C ratio ions is consistent with other field studies using the EESI-TOF, and suggests a higher contribution from aromatic precursors relative to the other OOA factors. The $(C_xH_yO_z)_{H:C\leq1.3}$ is consistent with that of aged wood burning factors retrieved during winter in Zurich (13-14%, Qi et al., 2019) (Fig. S19). Aged wood burning factors were also retrieved from source apportionment of wintertime EESI-TOF measurements in Magadino, located in a Swiss alpine valley (Stefenelli et al., *in prep*), where $(C_xH_yO_z)_{H:C\leq1.3}$ comprises 9.0-23.0 % of the total signal. Different from the aged biomass burning factors found in Zurich and Magadino, $C_6H_{10}O_5$ is not observed in MO-OOA$_{SFC}$, but other ions found in the aged biomass burning factors from Qi et al. (2019) and Stefenelli et al. (*in prep*) including $C_{10}H_{16}O_x$ ($x \geq 3$), are also apportioned to SFC-related factors in the present study. Still, the $C_xH_yO_z$ distribution in the MO-OOA$_{SFC}$ factor retrieved in Beijing differs from the previous studies in Switzerland in terms of the overall carbon number distribution. Specifically, the Swiss measurement in Magadino featured by biomass burning activities (Stefenelli et al., *in prep*) showed a peak at C_6 and a peak from C_8 to C_{10}, the chamber study on coal combustion oxidation (Amelie Bertrand, personal communication) exhibits a peak from C_6 to C_{12} whereas in Beijing the signal is spread over a much larger range (approximately C_7 to C_{19}).

Also evident from Fig. 7 is the high contribution from $C_xH_yO_zN_{1\text{-}2}$ ions, which comprise 45.5 % of the total signal. This is significantly higher than the 18-25 % observed in the Zurich factors by Qi et al. (2019) but comparable to 35-41 % observed in Magadino. As above, the carbon number distribution of $C_xH_yO_zN_{1\text{-}2}$ differs between Beijing and Switzerland, although the trends are reversed. In Beijing, the $C_xH_yO_zN_{1\text{-}2}$ signal occurs mostly in the C_6 to C_{10} range with a contribution of 73.0 % to total $C_xH_yO_zN_{1\text{-}2}$ signal, whereas for the Swiss measurements it spans C_6 to C_{10} with a contribution of 56 % at most to total $C_xH_yO_zN_{1\text{-}2}$ signal and almost evenly distributes into other bins. High intensity $C_xH_yO_zN_{1\text{-}2}$ ions in Beijing MO-OOA$_{SFC}$ include $C_6H_{11}NO_4$, $C_7H_{13}NO_4$, $C_8H_{15}NO_4$, $C_9H_{17}NO_4$ and $C_{10}H_{19}NO_4$. The high nitrogen content in MO-OOA$_{SFC}$ likely reflects high NO_x concentrations in the Beijing region during wintertime. In addition, ions tentatively attributed to nitrocatechol ($C_6H_5NO_4$) and its homologous series ($C_7H_7NO_4$, $C_8H_9NO_4$) are apportioned predominantly to this factor and CCOA (see Fig. S25b and Fig. S25c), indicating the influence of oxidised aromatics from coal combustion emissions (Mohr et al., 2013).

Interestingly, the AMS MO-OOA$_{SFC}$ profile and Van Krevelen plot (Fig. 9) show that the ions for which MO-OOA$_{SFC}$ has a high z-score (>1.5) predominantly exhibit low H:C ratios. These ions include $C_7H_2O^+$, $C_7H_3O^+$, $C_7H_4O^+$, $C_7H_5O^+$, $C_8H_4O^+$ and $C_8H_5O^+$. Although these ions are not addressed in OOA factor separation in most AMS PMF studies due to their low intensities, their high z-score in the present work suggests they may contain some source-specific information. The temporal evolution of these ions is consistent with EESI-TOF ions having a low H:C ratio and thus tentatively attributed to aromatics e.g., $C_{12}H_{10}O_8$ and $C_{16}H_{14}O_6$ (see Fig. S25d and Fig. S25e). This also suggests an elevated contribution from aromatic oxidation relative to the non-SFC-derived SOA factors. An increased contribution from EESI-TOF ions with low H:C was also observed in oxidised wood burning emissions by Qi et al. (2019).

3.3.3 LO-OOA$_{SFC}$

The LO-OOA$_{SFC}$ factor mass spectrum is also consistent with solid fuel combustion, but is less oxygenated than MO-OOA$_{SFC}$. The carbon number distribution of the EESI-TOF LO-OOA$_{SFC}$ mass spectrum (Fig. 7c) shows a contribution of $C_xH_yO_z$ ions with low H:C comparable to that of MO-OOA$_{SFC}$. Specifically, $(C_xH_yO_z)_{H:C\leq1.3}$ comprises 10.9 % of the total LO-OOA$_{SFC}$ signal, compared to 11.6 % from MO-OOA$_{SFC}$. This is consistent with less-aged biomass burning (LABB) factors retrieved from source apportionment of wintertime EESI-TOF data in Zurich and Magadino, where $(C_xH_yO_z)_{H:C\leq1.3}$ contributed 10-16 %. LO-OOA$_{SFC}$ contains a substantial contribution (10.5 %) from $C_6H_{10}O_5$ (levoglucosan and its isomers), which is substantially higher than that of MO-OOA$_{SFC}$ (0 %) and LO-OOA$_{ns}$ (0 %) and also than for primary BBOA (6.6 %) and CCOA (8.6 %). Interestingly, this factor has a very high fraction (31.8 %) from $(C_xH_yO_z)_{H:C\geq1.7}$, significantly higher than the 12 % to 14 % observed in Zurich and Magadino. It also has 18.9 % contribution from $(C_xH_yO_z)_{O:C\geq0.65}$, half of the fraction (~40 %) of the LABB factors in Zurich and Magadino. The high H:C (1.66) and low O:C (0.41) from EESI-TOF result in low averaged carbon oxidation states $\overline{OS}_{c}$ (-0.87) of this factor suggests this factor is less oxygenated than the LABB factors in those two studies, with lowest $\overline{OS}_{c}$ of -0.60.

Regarding nitrogen-containing species, $C_xH_yO_zN_{1\text{-}2}$ ions contribute 23.0 % to the total signal in this factor, similar to their contributions in the Zurich and Magadino LABB (17 % to 22 %). However, in Beijing a large fraction (10.7 %) of the $C_xH_yO_zN_{1\text{-}2}$ derives from a single ion ($C_6H_{11}NO_4$). Otherwise, the carbon number distribution of $C_xH_yO_zN_{1\text{-}2}$ ions in Beijing is weighted from C_7 to C_{10}, consistent with SOA from wood burning experiments with OH or NO_3 (Amelie Bertrand, personal communication) as shown in Fig. S28. Similar to the primary BBOA and CCOA factors, LO-OOA$_{SFC}$ is elevated overnight, suggesting a contribution from nighttime chemistry and/or rapid oxidation of primary emissions.

3.3.4 MO-OOA$_{aq}$

The MO-OOA$_{aq}$ factor time series is dominated by high absolute and relative concentrations during a haze event in the non-heating season. Both the atmospheric conditions during this event and the overall factor composition are consistent with a strong influence from SOA formed by aqueous phase chemistry.

Figure 10a shows the time series of the CO_2^+ and CO^+ ions from AMS, and the corresponding scatter plot is shown in Fig. 10b. For most of the data, the ratio of CO^+ to CO_2^+ is approximately 1, consistent with the mean CO^+/CO_2^+ value for bulk atmospheric OA (Canagaratna et al., 2015; Aiken et al., 2008) and the assumption in the standard AMS fragmentation table. In contrast, the CO^+/CO_2^+ slope is only 0.5 for the haze event on 4 to 7 November. This relative enhancement of CO_2^+ is characteristic of small acids or diacids, e.g., oxalic acid, malonic acid and succinic acid (Canagaratna et al., 2015), shown in Fig. S22. These molecules can enter the particle via solvation, potentially followed by aqueous-phase chemistry (Tan et al., 2012; Tan et al., 2010; Carlton et al., 2007; Ervens et al., 2004), or as condensation products of gas-phase reactions (Mehra et al., 2020; Wang et al., 2020; Zaytsev et al., 2019; Legrand et al., 2005; Sellegri et al., 2003; Sempere and Kawamura, 1994). For example, Lamkaddam et al. (2021) have shown that up to 70% of isoprene oxidation products can be dissolved in a water film. However, because aqueous reaction pathways under subsaturated conditions favor the uptake of highly soluble molecules such as small acids/diacids, their contribution relative to larger oxygenates is increased, consistent with the lower CO^+/CO_2^+ slope observed here.

An enhanced contribution from small acids is also suggested by the EESI-TOF MO-OOA$_{aq}$ profile. As shown in Fig. 7 and Fig. 8, MO-OOA$_{aq}$ has enhanced signal from ions with low carbon number relative to the other OOA factors. Further, Fig. 7 shows that these low-C ions are highly oxygenated (e.g., $C_6H_6O_5$), which is likewise consistent with small multifunctional acids and polyacids. The EESI-TOF spectra thus provide further support for the attribution of this factor to the processes discussed in the previous paragraph. However, the carbon number distribution in Fig. 7a shows $(C_xH_yO_z)_{H:C\leq1.3}$ comprises only 6.6 % to total signal, suggesting these acids are unlikely formed by oxidation of aromatic precursors. Note that due to the application of the volatility-based filter for distinguishing particle-phase vs. spurious ions (see section Text S3), the contribution of such small, highly oxygenated ions presented here represents a lower limit.

As shown in Fig. 3 and Fig. 11, MO-OOA$_{aq}$ provides a major fraction of 40.8 % to the total OA during the major haze event on 4 to 7 November (peak concentration > 40 $\mu g\ m^{-3}$). In fact, OA concentrations during this event are at least as high as those observed during the heating period, despite the likelihood of reduced concentrations of precursor VOCs due to the mandated reductions in combustion activities related to domestic heating in rural areas. We therefore investigate the reasons for the high SOA production during this specific event. The aerosol liquid water content (LWC) was calculated from ISORROPIA-II (Fountoukis and Nenes, 2007), and high LWC is typically associated with aqueous phase chemistry. The LWC concentration is presented in Fig. 10, together with the time series of MO-OOA$_{aq}$. The two time series are strongly correlated (r^2 = 0.93), and both are dramatically higher during the 4 to 7 November event than for the rest of the study, suggesting the role of the aqueous phase chemistry in this haze event. Note that the strong correlation between MO-OOA$_{aq}$ and LWC is not driven solely by the event on 4 to 7 November; rather, the two time series are remarkably well correlated throughout the entire campaign. This further supports the interpretation of MO-

OOA_{aq} as characteristic of aqueous SOA production throughout the campaign, rather than being characteristic of only a single event.

The question arises whether MO-OOA_{aq} reflects the irreversible production of SOA via aqueous pathways, or instead reversible solvation of volatile and semi-volatile organics. To assess this, we look in detail at the MO-OOA_{aq} and LWC correlations during the 4 to 7 November event (shown in Fig. 10) and change of MO-OOA_{aq} in every two-hour interval (Fig. S24). The most significant disagreement between the time series occurs from 08:00 to 23:00 on 6 November, when the LWC sharply decreases while MO-OOA_{aq} remains high. If MO-OOA_{aq} were driven by reversible solvation, this extended decrease in LWC would be expected to drive a corresponding decrease in MO-OOA_{aq}. However, the MO-OOA_{aq} concentrations appear unaffected by the decrease in LWC, suggesting that the MO-OOA_{aq} does indeed consist of irreversibly-generated SOA via aqueous chemistry.

The reasons for the high LWC are driven by the combination of high RH and high inorganic fraction (especially NH_4NO_3), which as shown in Fig. 1 are both maximised during this period. The high NH_4NO_3 content during 4 to 7 November is in turn driven by a unique airmass source region. Figure 12a shows 72-h backward trajectories calculated from the HYSPLIT transport model (Rolph et al., 2017; Stein et al., 2015), and analysed in Zefir v 4.0 (Petit et al., 2017). Trajectories are coloured by date and time. In the figure, trajectories from 4 to 7 November pass over regions of high NO_x emissions to the east and south of Beijing (Shandong and Henan provinces) before arriving at the sampling site. The air parcel spends approximately 30 hours over these high-NO_x regions, as shown in Fig. 12b. As shown in Fig. S29, the period of 4 to 7 November is the only time in the campaign where the back trajectories pass over this region. Due to the high NO_2 concentration and high RH in this period, particulate nitrate is produced during this regional transport homogeneously and/or heterogeneously, resulting in water uptake and high LWC in the aerosol phase. The high LWC in turn facilitates further heterogeneous formation of nitrate. This positive feedback provides favorable conditions for efficient aqueous chemistry and thus production of MO-OOA_{aq} (Kuang et al., 2020).

3.3.5 LO-OOA_{ns}

In Sect. 3.2, this factor has been identified as LO-OOA because of its moderately high CO_2^+ signal and non-negligible contribution from the C_xH_y group. The time series of this factor shows clear diurnal variation which peaks at around 20:00 in the non-heating season (Fig. 3a and 3c), but this variation is not clear in the heating season. In addition, the contribution of this factor to total OA is higher in the clean period than during the haze events (Fig. 3b), indicating this may be related to regional sources/processes rather than more local SFC emissions. The diurnal cycle of this factor is similar to COA and LO-OOA_{SFC}, but the chemical characteristics of these three factors are different. Compared to LO-OOA_{SFC}, this factor is characterised by ions with high H:C and low O:C and does not have a significant contribution from $C_6H_{10}O_5$, a key ion in SFC-related LO-OOAs identified in both the present and previous studies (Qi et al., 2019; Stefenelli et al., *in prep*). LO-OOA_{ns} also does not have large contributions from ions with the aromatic feature of low H:C. Although the spectrum of COA is also characterised by ions with high H:C and low O:C, the carbon number distribution plots of COA are characterised by significant signal from long-chain acids at high carbon number, whereas the carbon number distribution of this factor is characterised by high signal at low carbon number (from C_8 to C_{12}). Compared to other OOA factors, this factor has the lowest O:C ratio (0.33) and highest H:C ratio (1.69) from EESI-TOF. Since it is not characterised by any source-specific ions or signatures identified in previous EESI-TOF studies (e.g., levoglucosan and its isomers), this factor is named as LO-OOA_{ns}, representing non-source-specific LO-OOA.

4. Atmospheric implications

As discussed in Sect. 3.1, meteorological conditions are responsible for an alternating occurrence of haze and clean periods and these effects from meteorology are well-understood (Duan et al., 2020; Duan et al., 2019; Zhao et al., 2019; Xu et al., 2019; Sun et al., 2016a; Sun et al., 2016b). In addition, meteorology can also influence air mass trajectories on the regional/mesoscale, which may further influence the aerosol chemical composition. By comparing measurements before and after the start of the heating season (15 November), the effects of heating emissions on clean and haze periods in Beijing can be assessed. Figure 11 shows the time series of total OA and the contribution of different factors to each haze event. Systematic differences between seasons suggest the influences of different sources/processes.

Clean periods in both the non-heating and heating seasons are dominated by SOA, comprising 76.9 % in the non-heating season and 70.3 % in the heating season. In both seasons, the single largest component is LO-OOA_{ns} (45.3 % and 33.2 % in the non-heating and heating seasons, respectively), consistent with its identification as regional SOA not specific to a single emissions source. The SFC fraction is higher in the heating season, with CCOA and BBOA jointly comprising 22.7 % (vs. 15.0 % in the non-heating season) and LO-OOA_{SFC} and MO-OOA_{SFC} jointly comprising 25.1 % (vs. 19.2 % non-heating season).

Seasonal differences become more pronounced under haze conditions. Three light haze events (maximum concentrations between 15.4 and 30.8 µg m^{-3}) were observed in each season. During these events in the non-heating season, LO-OOA_{ns} remains the single largest component (33.0 to 42.7 %), although its fraction is slightly reduced relative to clean conditions (45.3 %). There is no corresponding fractional increase observed in any of the other factors, but rather an across-the-board relative increase in all, which results in a slightly increased POA fraction (ranging from 29.1 to 37.5 %, vs. 23.1 % under clean conditions). These changes likely result from an increased role of local emissions and reactivity under the stagnant conditions giving rise to haze. The non-heating light haze events contrast strongly with the heating light haze, where there is a larger reduction in the LO-OOA_{ns} fraction (at least 33.0 % in non-heating season to at most 29.6 % in heating season) that corresponds specifically to increased SFC POA (at most 26.7 % in non-heating season to at least 27.5 % in heating season). Interestingly, the SFC SOA fraction is not significantly higher than under clean conditions, although event-to-event variation is large (ranging from 20.3 % to 41.0 % under heating season haze vs 25.1 % under clean conditions).

In general, the light haze events within a given season are relatively similar to each other. However, significant differences in composition are observed between the light and severe haze events within a given season. The two severe haze events occurring within the heating season are also quite different from each other. The conclusions that can be drawn from this observation are limited by the small number of severe haze events sampled (1 non-heating, 2 heating), but suggest the potential for unique meteorological/transport phenomena that may affect sources and composition during the most extreme events. For example, the non-heating haze event (4 to 7 Nov.) is dominated by MO-OOA_{aq} from aqueous processes (40.8 % of OA), and as discussed in the previous section corresponds to unique airmass back-trajectories over high-NO_x regions. The event from 18 to 22 Nov. is dominated by SFC, especially BBOA, which comprises 35.8 % of OA (with CCOA contributing an additional 12.5 %), while SFC SOA comprises an only slightly larger fraction (27.8 % of OA) than under clean conditions. In contrast, the severe haze event from 30 Nov. to 3 Dec. has a large contribution from both SFC POA (32.8 %) and SFC SOA (41.0 %). Interestingly, the temporal evolution of these two events is also different, with the 18 to 22 Nov. event (high SFC POA) commencing with a sudden concentration increase but remaining relatively stable thereafter, while concentrations during the 30 Nov. to 3 Dec. event (high SFC POA and SOA) increase gradually over multiple days. However, a close inspection of the 18 to 22 Nov. event in Fig. 3b shows a decrease in the BBOA fraction and increase in MO-OOA_{SFC} as the event proceeds, suggesting a generally important role for local SOA formation in a stagnant airmass during the course of a haze event.

As a conclusion, our observation suggests that the sources and processes giving rise to haze events in Beijing are variable and seasonally-dependent. Two salient features are: 1) in the heating season, SOA formation is driven by oxidation of aromatics from solid fuel combustion, with secondary SFC-related factors (i.e., sum of MO-OOA_{SFC} and LO-OOA_{SFC}) contributing 37.2 % to 72.8 % of total SOA, and 2) under high NO_x and RH conditions, aqueous phase chemistry may make a major contribution to SOA formation (with MO-OOA_{aq} comprising 53.7 % of total SOA). The combination of high inorganic content and aqueous SOA can yield total mass concentrations comparable to those observed in the heating season, despite reduced regional VOC emissions in the absence of heating processes.

Our back-trajectory analysis shows that from 4 to 7 November, the air masses passed through a high NO_2 concentration region and remained for more than 24 hours in this region (Fig. 12), which facilitated nitrate formation in the aerosol phase and thus water uptake. Therefore, our observation suggests that meteorology cannot only influence the haze evolution on a local scale, but also can have significant effect on aerosol chemistry and chemical composition by influencing the origin and pathway of air mass.

From a technical perspective, a surprising outcome of this source apportionment analysis was the extent to which the AMS SOA factor profiles contained source-related information corroborating the chemically more specific measurements of the EESI-TOF. Specifically, the SFC-related factors exhibited systematic enhancements in ions with low H:C ratios, while the CO^+/CO_2^+ ratio clearly higher than 1 was found to be a clear indicator for aqueous-phase chemical processing. Although the latter observation requires the improved mass resolution of the L-TOF-AMS and is therefore not retrievable from most existing AMS datasets, taken together they suggest that AMS SOA spectra may contain more source-specific information than is typically recognised. Although these results represent a single case study and so should not be overinterpreted, we suggest that intensity-independent statistical tools such as the z-score analysis employed here may be effective in retrieving such information and in providing additional insight into SOA sources. The combination of quantitative AMS data with semi-quantitative EESI-TOF measurements is also shown to be promising, and alternative methods for combining such datasets (e.g., as discussed in the Methods section) should be pursued.

5. Conclusions

OA sources were investigated in Beijing during an intensive field deployment of AMS and EESI-TOF instruments from late September to mid-December 2017, covering the transition from the non-heating to heating seasons. This represents the first deployment of the EESI-TOF in a heavily polluted city. The robust quantification of the AMS and high chemical resolution of the EESI-TOF are shown to be highly complementary, facilitating identification of the sources and processes governing SOA concentrations. An integrated source apportionment study was conducted, by the application of PMF to AMS-only data to determine factor time series, followed by PMF on EESI-TOF-only data using AMS-derived factor time series as constraints, to increase the chemical information associated with each factor. facilitate chemical interpretation of the AMS-determined factors by using z-score analysis and carbon number distribution plots, which successfully resolved and interpreted four SOA sources and processes.

The source apportionment analysis yielded four primary factors and four secondary factors. Primary factors were hydrocarbon-like OA (HOA) characterised by a high fraction of hydrocarbon fragments, cooking-related OA (COA) characterised by long-chain fatty acids, biomass burning OA (BBOA) with a high contribution from levoglucosan, and coal combustion OA (CCOA) with a high PAH signal at high *m/z* range. The secondary factors consisted of more- and less-oxygenated oxygenated organic aerosol from solid fuel combustion (MO-OOA_{SFC} and LO-OOA_{SFC}), more-oxygenated aerosol from aqueous-phase chemistry (MO-OOA_{aq}), and less-oxygenated OA from mixed or indeterminate sources (LO-OOA_{ns}). The SFC-related factors were characterised by a low H:C ratio in both the EESI-TOF and AMS spectra and increased concentrations during the heating period. MO-OOA_{aq} was characterised by an increased contribution from small, highly oxygenated ions and a low AMS CO^+/CO_2^+ ratio; taken together, these observations suggest an enhanced contribution from small acids and diacids.

The OA composition in Beijing is dominated by organic aerosols, with a significant SOA fraction (66.4±13.5 %) to total OA throughout the campaign. SOA formation during the heating season derives mainly from solid fuel combustion. However, even during the non-heating season when solid fuel combustion was not a major source, an intense haze event was observed with OA concentrations comparable to the highest concentrations observed during the heating season. These high concentrations were due to significant SOA production from aqueous phase chemistry, and corresponded to the passage of air parcels over the high NO_x regions to the east and south of Beijing. This suggests that aqueous chemistry may provide a major contribution to SOA formation under certain meteorological conditions, even during periods of intense haze.

Data Availability. The data presented in the text and figures will be available at the Zenodo Online repository (https://zenodo.org) upon final publication.

Competing interests. The authors declare that they have no conflict of interest.

Author contributions. JGS, ASHP, JC and RJH initiated the experiment. YT was in charge of the Beijing campaign. JD, YG, and HZ provided necessary coordination during the campaign. YT, VP, LQ, JD, YG, VK, PR, GS, LW, YW, HZ and JGS DMB were involved in the measurement campaign. YT mainly analysed the AMS and EESI-TOF data and performed PMF analysis. VP, LQ and GS provided supports for AMS and EESI-TOF data analysis and PMF interpreation. LW, PR, HZ, RJH and JC provided data collected from supporting measurements. All authors from PSI contributed to the data interpretation. All authors contributed to the manuscript revision.

Acknowledgements. We gratefully acknowledge the contribution from Dr. LIU Fei from NASA for providing NO_x emission map of China. We also acknowledge the NOAA Air Resources Laboratory (ARL) for the provision of the HYSPLIT transport and dispersion model and READY website (https://www.ready.noaa.gov) used in this publication. Logistical support by André TEIXEIRA (Paul Scherrer Institut) and Dr. WU Yunfei (Institute of Atmospheric Physics, Chinese Academy of Sciences), and coordination support by Prof. CHEN Chunying (National Center for Nanoscience and Technology, Chinese Academy of Sciences) are gratefully acknowledged.

Financial support. This study was funded by the Swiss National Science Foundation starting grant BSSGI0_155846 (IPR-SHOP), the EU Horizon 2020 Framework Programme via the ERA-PLANET project SMURBS (grant agreement no. 689443), the National Research Program for Key Issues in Air Pollution Control (DQGG0105), the Natural National Science Foundation (21661132005), the National Natural Science Foundation of China (NSFC) under grant no. 41925015 and the Chinese Academy of Sciences (no. ZDBS-LY-DQC001).

Reference

Äijälä, M., Heikkinen, L., Fröhlich, R., Canonaco, F., Prévôt, A. S. H., Junninen, H., Petäjä, T., Kulmala, M., Worsnop, D., and Ehn, M.: Resolving anthropogenic aerosol pollution types – deconvolution and exploratory classification of pollution events, Atmos. Chem. Phys., 17, 3165-3197, https://doi.org/10.5194/acp-17-3165-2017, 2017.

Aiken, A. C., Decarlo, P. F., Kroll, J. H., Worsnop, D. R., Huffman, J. A., Docherty, K. S., Ulbrich, I. M., Mohr, C., Kimmel, J. R., Sueper, D., Sun, Y., Zhang, Q., Trimborn, A., Northway, M., Ziemann, P. J., Canagaratna, M. R., Onasch, T. B., Alfarra, M. R., Prevot, A. S. H., Dommen, J., Duplissy, J., Metzger, A., Baltensperger, U., and Jimenez, J. L.: O/C and OM/OC ratios of primary, secondary, and ambient organic aerosols with high-resolution time-of-flight aerosol mass spectrometry, Environ Sci Technol, 42, 4478-4485, https://doi.org/10.1021/es703009q, 2008.

Alfarra, M. R., Prevot, A. S. H., Szidat, S., Sandradewi, J., Weimer, S., Lanz, V. A., Schreiber, D., Mohr, M., and Baltensperger, U.: Identification of the mass spectral signature of organic aerosols from wood burning emissions, Environ Sci Technol, 41, 5770-5777, https://doi.org/10.1021/es062289b, 2007.

Allan, J. D., Alfarra, M. R., Bower, K. N., Williams, P. I., Gallagher, M. W., Jimenez, J. L., McDonald, A. G., Nemitz, E., Canagaratna, M. R., Jayne, J. T., Coe, H., and Worsnop, D. R.: Quantitative sampling using an Aerodyne aerosol mass spectrometer: 2. Measurements of fine particulate chemical composition in two UK cities J Geophys Res-Atmos, 108, 4091, https://doi.org/10.1029/2002JD002359, 2003a.

Allan, J. D., Jimenez, J. L., Williams, P. I., Alfarra, M. R., Bower, K. N., Jayne, J. T., Coe, H., and Worsnop, D. R.: Quantitative sampling using an Aerodyne aerosol mass spectrometer: 1. Techniques of data interpretation and error analysis (vol 108, art no 4090, 2003), J Geophys Res-Atmos, 108, 4090, https://doi.org/10.1029/2002JD002358, 2003b.

An, Z., Huang, R.-J., Zhang, R., Tie, X., Li, G., Cao, J., Zhou, W., Shi, Z., Han, Y., Gu, Z., and Ji, Y.: Severe haze in northern China: A synergy of anthropogenic emissions and atmospheric processes, Proceedings of the National Academy of Sciences, 116, 8657-8666, https://doi.org/10.1073/pnas.1900125116, 2019.

Beelen, R., Raaschou-Nielsen, O., Stafoggia, M., Andersen, Z. J., Weinmayr, G., Hoffmann, B., Wolf, K., Samoli, E., Fischer, P., Nieuwenhuijsen, M., Vineis, P., Xun, W. W., Katsouyanni, K., Dimakopoulou, K., Oudin, A., Forsberg, B., Modig, L., Havulinna, A. S., Lanki, T., Turunen, A., Oftedal, B., Nystad, W., Nafstad, P., De Faire, U., Pedersen, N. L., Ostenson, C. G., Fratiglioni, L., Penell, J., Korek, M., Pershagen, G., Eriksen, K. T., Overvad, K., Ellermann, T., Eeftens, M., Peeters, P. H., Meliefste, K., Wang, M., Bueno-de-Mesquita, B., Sugiri, D., Kramer, U., Heinrich, J., de Hoogh, K., Key, T., Peters, A., Hampel, R., Concin, H., Nagel, G., Ineichen, A., Schaffner, E., Probst-Hensch, N., Kunzli, N., Schindler, C., Schikowski, T., Adam, M., Phuleria, H., Vilier, A., Clavel-Chapelon, F., Declercq, C., Grioni, S., Krogh, V., Tsai, M. Y., Ricceri, F., Sacerdote, C., Galassi, C., Migliore, E., Ranzi, A., Cesaroni, G., Badaloni, C., Forastiere, F., Tamayo, I., Amiano, P., Dorronsoro, M., Katsoulis, M., Trichopoulou, A., Brunekreef, B., and Hoek, G.: Effects of long-term exposure to air pollution on natural-cause mortality: an analysis of 22 European cohorts within the multicentre ESCAPE project, Lancet, 383, 785-795, https://doi.org/10.1016/S0140-6736(13)62158-3, 2014.

Beijing achieves air quality goal in 2017: http://english.www.gov.cn/news/top_news/2018/01/03/content_281476000086408.htm, access: 22 February, 2018

Bozzetti, C., Sosedova, Y., Xiao, M., Daellenbach, K. R., Ulevicius, V., Dudoitis, V., Mordas, G., Bycenkiene, S., Bycenkiene, S., Plauskaite, K., Vlachou, A., Golly, B., Chazeau, B., Besombes, J. L., Baltensperger, U., Jaffrezo, J. L., Slowik, J. G., El Haddad, I., and Prevot, A. S. H.: Argon offline-AMS source apportionment of organic aerosol over yearly cycles for an urban, rural, and marine site in northern Europe, Atmos Chem Phys, 17, 117-141, https://doi.org/10.5194/acp-17-117-2017, 2017.

Budisulistiorini, S. H., Canagaratna, M. R., Croteau, P. L., Marth, W. J., Baumann, K., Edgerton, E. S., Shaw, S. L., Knipping, E. M., Worsnop, D. R., Jayne, J. T., Gold, A., and Surratt, J. D.: Real-Time Continuous Characterization of Secondary Organic Aerosol Derived from Isoprene Epoxydiols in Downtown Atlanta, Georgia, Using the Aerodyne Aerosol Chemical Speciation Monitor, Environ Sci Technol, 47, 5686-5694, https://doi.org/10.1021/es400023n, 2013.

Brown, W. L., Day, D. A., Stark, H., Pagonis, D., Krechmer, J. E., Liu, X., Price, D. J., Katz, E. F., DeCarlo, P. F., Masoud, C. G., Wang, D. S., Hildebrandt Ruiz, L., Arata, C., Lunderberg, D. M., Goldstein, A. H., Farmer, D. K., Vance, M. E., and Jimenez, J. L.: Real-time organic aerosol chemical speciation in the indoor environment using extractive electrospray ionization mass spectrometry, Indoor Air, 31, 141-155, https://doi.org/10.1111/ina.12721, 2021.

Bryant, D. J., Dixon, W. J., Hopkins, J. R., Dunmore, R. E., Pereira, K. L., Shaw, M., Squires, F. A., Bannan, T. J., Mehra, A., Worrall, S. D., Bacak, A., Coe, H., Percival, C. J., Whalley, L. K., Heard, D. E., Slater, E. J., Ouyang, B., Cui, T., Surratt, J. D., Liu, D., Shi, Z., Harrison, R., Sun, Y., Xu, W., Lewis, A. C., Lee, J. D., Rickard, A. R., and Hamilton, J. F.: Strong anthropogenic control of secondary organic aerosol formation from isoprene in Beijing, Atmos. Chem. Phys., 20, 7531-7552, https://doi.org/10.5194/acp-20-7531-2020, 2020.

Canagaratna, M. R., Jayne, J. T., Jimenez, J. L., Allan, J. D., Alfarra, M. R., Zhang, Q., Onasch, T. B., Drewnick, F., Coe, H., Middlebrook, A., Delia, A., Williams, L. R., Trimborn, A. M., Northway, M. J., DeCarlo, P. F., Kolb, C. E., Davidovits, P., and Worsnop, D. R.: Chemical and microphysical characterization of ambient aerosols with the aerodyne aerosol mass spectrometer, Mass Spectrom Rev, 26, 185-222, https://doi.org/10.1002/mas.20115, 2007.

Canagaratna, M. R., Jimenez, J. L., Kroll, J. H., Chen, Q., Kessler, S. H., Massoli, P., Hildebrandt Ruiz, L., Fortner, E., Williams, L. R., Wilson, K. R., Surratt, J. D., Donahue, N. M., Jayne, J. T., and Worsnop, D. R.: Elemental ratio measurements of organic compounds using aerosol mass spectrometry: characterization, improved calibration, and implications, Atmos Chem Phys, 15, 253-272, https://doi.org/10.5194/acp-15-253-2015, 2015.

Canonaco, F., Crippa, M., Slowik, J. G., Baltensperger, U., and Prevot, A. S. H.: SoFi, an IGOR-based interface for the efficient use of the generalized multilinear engine (ME-2) for the source apportionment: ME-2 application to aerosol mass spectrometer data, Atmos Meas Tech, 6, 3649-3661, https://doi.org/10.5194/amt-6-3649-2013, 2013.

Carlton, A. G., Turpin, B. J., Altieri, K. E., Seitzinger, S., Reff, A., Lim, H. J., and Ervens, B.: Atmospheric oxalic acid and SOA production from glyoxal: Results of aqueous photooxidation experiments, Atmospheric Environment, 41, 7588-7602, https://doi.org/10.1016/j.atmosenv.2007.05.035, 2007.

Chan, Y. C., Hawas, O., Hawker, D., Vowles, P., Cohen, D. D., Stelcer, E., Simpson, R., Golding, G., and Christensen, E.: Using multiple type composition data and wind data in PMF analysis to apportion and locate sources of air pollutants, Atmospheric Environment, 45, 439-449, https://doi.org/10.1016/j.atmosenv.2010.09.060, 2011.

Chow, J. C., Bachmann, J. D., Wierman, S. S. G., Mathai, C. V., Malm, W. C., White, W. H., Mueller, P. K., Kumar, N., and Watson, J. G.: Visibility: Science and regulation - Discussion, J Air Waste Manage, 52, 973-999, https://doi.org/10.1016/j.atmosenv.2010.09.060, 2002.

Crippa, M., El Haddad, I., Slowik, J. G., DeCarlo, P. F., Mohr, C., Heringa, M. F., Chirico, R., Marchand, N., Sciare, J., Baltensperger, U., and Prévôt, A. S. H.: Identification of marine and continental aerosol sources in Paris using high resolution aerosol mass spectrometry, Journal of Geophysical Research: Atmospheres, 118, 1950-1963, https://doi.org/10.1002/jgrd.50151, 2013.

Crippa, M., Canonaco, F., Lanz, V. A., Aijala, M., Allan, J. D., Carbone, S., Capes, G., Ceburnis, D., Dall'Osto, M., Day, D. A., DeCarlo, P. F., Ehn, M., Eriksson, A., Freney, E., Hildebrandt Ruiz, L., Hillamo, R., Jimenez, J. L., Junninen, H., Kiendler-Scharr, A., Kortelainen, A. M., Kulmala, M., Laaksonen, A., Mensah, A., Mohr, C., Nemitz, E., O'Dowd, C., Ovadnevaite, J., Pandis, S. N., Petaja, T., Poulain, L., Saarikoski, S., Sellegri, K., Swietlicki, E., Tiitta, P., Worsnop, D. R., Baltensperger, U., and Prevot, A. S. H.: Organic aerosol components derived from 25 AMS data sets across Europe using a consistent ME-2 based source apportionment approach, Atmos Chem Phys, 14, 6159-6176, https://doi.org/10.5194/acp-14-6159-2014, 2014.

Daellenbach, K. R., Stefenelli, G., Bozzetti, C., Vlachou, A., Fermo, P., Gonzalez, R., Piazzalunga, A., Colombi, C., Canonaco, F., Hueglin, C., Kasper-Giebl, A., Jaffrezo, J. L., Bianchi, F., Slowik, J. G., Baltensperger, U., El-Haddad, I., and Prevot, A. S. H.: Long-term chemical analysis and organic aerosol source apportionment at nine sites in central Europe: source identification and uncertainty assessment, Atmos Chem Phys, 17, 13265-13282, https://doi.org/10.5194/acp-17-13265-2017, 2017.

Daellenbach, K. R., Uzu, G., Jiang, J., Cassagnes, L.-E., Leni, Z., Vlachou, A., Stefenelli, G., Canonaco, F., Weber, S., Segers, A., Kuenen, J. J. P., Schaap, M., Favez, O., Albinet, A., Aksoyoglu, S., Dommen, J., Baltensperger, U., Geiser, M., El Haddad, I., Jaffrezo, J.-L., and Prévôt, A. S. H.: Sources of particulate-matter air pollution and its oxidative potential in Europe, Nature, 587, 414-419, https://doi.org/10.1038/s41586-020-2902-8, 2020.

Davison, A. C., and Hinkley, D. V.: Bootstrap methods and their application, Cambridge University Press, Cambridge, New York, NY, USA, 1997.

DeCarlo, P. F., Kimmel, J. R., Trimborn, A., Northway, M. J., Jayne, J. T., Aiken, A. C., Gonin, M., Fuhrer, K., Horvath, T., Docherty, K. S., Worsnop, D. R., and Jimenez, J. L.: Field-deployable, high-resolution, time-of-flight aerosol mass spectrometer, Anal Chem, 78, 8281-8289, https://doi.org/10.1021/ac061249n, 2006.

Duan, J., Huang, R. J., Lin, C., Dai, W., Wang, M., Gu, Y., Wang, Y., Zhong, H., Zheng, Y., Ni, H., Dusek, U., Chen, Y., Li, Y., Chen, Q., Worsnop, D. R., O'Dowd, C. D., and Cao, J.: Distinctions in source regions and formation mechanisms of secondary aerosol in Beijing from summer to winter, Atmos. Chem. Phys., 19, 10319-10334, https://doi.org/10.5194/acp-19-10319-2019, 2019.

Duan, J., Huang, R. J., Li, Y., Chen, Q., Zheng, Y., Chen, Y., Lin, C., Ni, H., Wang, M., Ovadnevaite, J., Ceburnis, D., Chen, C., Worsnop, D. R., Hoffmann, T., O'Dowd, C., and Cao, J.: Summertime and wintertime atmospheric processes of secondary aerosol in Beijing, Atmos. Chem. Phys., 20, 3793-3807, https://doi.org/10.5194/acp-20-3793-2020, 2020.

Dzepina, K., Arey, J., Marr, L. C., Worsnop, D. R., Salcedo, D., Zhang, Q., Onasch, T. B., Molina, L. T., Molina, M. J., and Jimenez, J. L.: Detection of particle-phase polycyclic aromatic hydrocarbons in Mexico City using an aerosol mass spectrometer, Int J Mass Spectrom, 263, 152-170, https://doi.org/10.1016/j.ijms.2007.01.010, 2007.

Eichler, P., Müller, M., D'Anna, B., and Wisthaler, A.: A novel inlet system for online chemical analysis of semi-volatile submicron particulate matter, Atmos. Meas. Tech., 8, 1353-1360, https://doi.org/10.5194/amt-8-1353-2015, 2015.

Elser, M., Huang, R. J., Wolf, R., Slowik, J. G., Wang, Q. Y., Canonaco, F., Li, G. H., Bozzetti, C., Daellenbach, K. R., Huang, Y., Zhang, R. J., Li, Z. Q., Cao, J. J., Baltensperger, U., El-Haddad, I., and Prevot, A. S. H.: New insights into PM2.5 chemical composition and sources in two major cities in China during extreme haze events using aerosol mass spectrometry, Atmos Chem Phys, 16, 3207-3225, https://doi.org/10.5194/acp-16-3207-2016, 2016.

Ervens, B., Feingold, G., Frost, G. J., and Kreidenweis, S. M.: A modeling study of aqueous production of dicarboxylic acids: 1. Chemical pathways and speciated organic mass production, J Geophys Res-Atmos, 109, D15205, https://doi.org/10.1029/2003JD004387, 2004.

Feng, T., Zhao, S., Bei, N., Wu, J., Liu, S., Li, X., Liu, L., Qian, Y., Yang, Q., Wang, Y., Zhou, W., Cao, J., and Li, G.: Secondary organic aerosol enhanced by increasing atmospheric oxidizing capacity in Beijing–Tianjin–Hebei (BTH), China, Atmos. Chem. Phys., 19, 7429-7443, https://doi.org/10.5194/acp-19-7429-2019, 2019.

Fenger, J.: Urban air quality, Atmospheric Environment, 33, 4877-4900, https://doi.org/10.1016/S1352-2310(99)00290-3, 1999.

Forster, P., Ramaswamy, V., Artaxo, P., Berntsen, T., Betts, R., Fahey, D.W., Haywood, J., Lean, J., Lowe, D.C., Myhre, G., Nganga, J., Prinn, R., Raga, G., Schulz, M. and Van Dorland, R.: Changes in Atmospheric Constituents and in Radiative Forcing. In: Climate Change 2007: The Physical Science Basis. Contribution of Working Group I to the Fourth Assessment Report of the Intergovernmental Panel on Climate Change [Solomon, S., Qin, D., Manning, M., Chen, Z., Marquis, M., Averyt, K.B., Tignor, M. and Miller, H.L. (eds.)]. Cambridge University Press, Cambridge, United Kingdom and New York, NY, USA, 2007.

Fountoukis, C. and Nenes, A.: ISORROPIA II: a computationally efficient thermodynamic equilibrium model for K^+–Ca^{2+}–Mg^{2+}–NH_4^+–Na^+–SO_4^{2-}–NO_3^-–Cl^-–H_2O aerosols, Atmos. Chem. Phys., 7, 4639–4659, https://doi.org/10.5194/acp-7-4639-2007, 2007.

Freney, E., Zhang, Y. J., Croteau, P., Amodeo, T., Williams, L., Truong, F., Petit, J. E., Sciare, J., Sarda-Esteve, R., Bonnaire, N., Arumae, T., Aurela, M., Bougiatioti, A., Mihalopoulos, N., Coz, E., Artinano, B., Crenn, V., Elste, T., Heikkinen, L., Poulain, L., Wiedensohler, A., Herrmann, H., Priestman, M., Alastuey, A., Stavroulas, I., Tobler, A., Vasilescu, J., Zanca, N., Canagaratna, M., Carbone, C., Flentje, H., Green, D., Maasikmets, M., Marmureanu, L., Minguillon, M. C., Prevot, A. S. H., Gros, V., Jayne, J., and Favez, O.: The second ACTRIS inter-comparison (2016) for Aerosol Chemical Speciation Monitors (ACSM): Calibration protocols and instrument performance evaluations, Aerosol Sci Tech, 53, 830-842, https://doi.org/10.1080/02786826.2019.1608901, 2019.

Ge, X. L., Setyan, A., Sun, Y. L., and Zhang, Q.: Primary and secondary organic aerosols in Fresno, California during wintertime: Results from high resolution aerosol mass spectrometry, J Geophys Res-Atmos, 117, D19201, https://doi.org/10.1029/2012JD018026, 2012.

Halliwell, B., and Cross, C. E.: Oxygen-Derived Species - Their Relation to Human-Disease and Environmental-Stress, Environ Health Persp, 102, 5-12, https://doi.org/10.1289/ehp.94102s105, 1994.

Hallquist, M., Wenger, J. C., Baltensperger, U., Rudich, Y., Simpson, D., Claeys, M., Dommen, J., Donahue, N. M., George, C., Goldstein, A. H., Hamilton, J. F., Herrmann, H., Hoffmann, T., Iinuma, Y., Jang, M., Jenkin, M. E., Jimenez, J. L., Kiendler-Scharr, A., Maenhaut, W., McFiggans, G., Mentel, T. F., Monod, A., Prevot, A. S. H., Seinfeld, J. H., Surratt, J. D., Szmigielski, R., and Wildt, J.: The formation, properties and impact of secondary organic aerosol: current and emerging issues, Atmos Chem Phys, 9, 5155-5236, https://doi.org/10.5194/acp-9-5155-2009, 2009.

Han, S., Kondo, Y., Oshima, N., Takegawa, N., Miyazaki, Y., Hu, M., Lin, P., Deng, Z., Zhao, Y., Sugimoto, N., and Wu, Y.: Temporal variations of elemental carbon in Beijing, J Geophys Res-Atmos, 114, D23202, https://doi.org/10.1029/2009JD012027, 2009.

Hildebrandt, L., Engelhart, G. J., Mohr, C., Kostenidou, E., Lanz, V. A., Bougiatioti, A., DeCarlo, P. F., Prevot, A. S. H., Baltensperger, U., Mihalopoulos, N., Donahue, N. M., and Pandis, S. N.: Aged organic aerosol in the Eastern Mediterranean: the Finokalia Aerosol Measurement Experiment-2008, Atmos Chem Phys, 10, 4167-4186, https://doi.org/10.5194/acp-10-4167-2010, 2010.

Hu, W. W., Hu, M., Yuan, B., Jimenez, J. L., Tang, Q., Peng, J. F., Hu, W., Shao, M., Wang, M., Zeng, L. M., Wu, Y. S., Gong, Z. H., Huang, X. F., and He, L. Y.: Insights on organic aerosol aging and the influence of coal combustion at a regional receptor site of central eastern China, Atmos. Chem. Phys., 13, 10095-10112, https://doi.org/10.5194/acp-13-10095-2013, 2013.

Hu, W. W., Hu, M., Hu, W., Jimenez, J. L., Yuan, B., Chen, W. T., Wang, M., Wu, Y. S., Chen, C., Wang, Z. B., Peng, J. F., Zeng, L. M., and Shao, M.: Chemical composition, sources, and aging process of submicron aerosols in Beijing: Contrast between summer and winter, J Geophys Res-Atmos, 121, 1955-1977, https://doi.org/10.1002/2015JD024020, 2016.

Huang, R. J., Zhang, Y. L., Bozzetti, C., Ho, K. F., Cao, J. J., Han, Y. M., Daellenbach, K. R., Slowik, J. G., Platt, S. M., Canonaco, F., Zotter, P., Wolf, R., Pieber, S. M., Bruns, E. A., Crippa, M., Ciarelli, G., Piazzalunga, A., Schwikowski, M., Abbaszade, G., Schnelle-Kreis, J., Zimmermann, R., An, Z. S., Szidat, S., Baltensperger, U., El Haddad, I., and Prevot, A. S. H.: High secondary aerosol contribution to particulate pollution during haze events in China, Nature, 514, 218-222, https://doi.org/10.1038/nature13774, 2014.

Huang, X. F., He, L. Y., Hu, M., Canagaratna, M. R., Sun, Y., Zhang, Q., Zhu, T., Xue, L., Zeng, L. W., Liu, X. G., Zhang, Y. H., Jayne, J. T., Ng, N. L., and Worsnop, D. R.: Highly time-resolved chemical characterization of atmospheric submicron particles during 2008 Beijing Olympic Games using an Aerodyne High-Resolution Aerosol Mass Spectrometer, Atmos Chem Phys, 10, 8933-8945, https://doi.org/10.5194/acp-10-8933-2010, 2010.

Jimenez, J. L., Canagaratna, M. R., Donahue, N. M., Prevot, A. S. H., Zhang, Q., Kroll, J. H., DeCarlo, P. F., Allan, J. D., Coe, H., Ng, N. L., Aiken, A. C., Docherty, K. S., Ulbrich, I. M., Grieshop, A. P., Robinson, A. L., Duplissy, J., Smith, J. D., Wilson, K. R., Lanz, V. A., Hueglin, C., Sun, Y. L., Tian, J., Laaksonen, A., Raatikainen, T., Rautiainen, J., Vaattovaara, P., Ehn, M., Kulmala, M., Tomlinson, J. M., Collins, D. R., Cubison, M. J., Dunlea, E. J., Huffman, J. A., Onasch, T. B., Alfarra, M. R., Williams, P. I., Bower, K., Kondo, Y., Schneider, J., Drewnick, F., Borrmann, S., Weimer, S., Demerjian, K., Salcedo, D., Cottrell, L., Griffin, R., Takami, A., Miyoshi, T., Hatakeyama, S., Shimono, A., Sun, J. Y., Zhang, Y. M., Dzepina, K., Kimmel, J. R., Sueper, D., Jayne, J. T., Herndon, S. C., Trimborn, A. M., Williams, L. R., Wood, E. C., Middlebrook, A. M., Kolb, C. E., Baltensperger, U., and Worsnop, D. R.: Evolution of Organic Aerosols in the Atmosphere, Science, 326, 1525-1529, https://doi.org/10.1126/science.1180353, 2009.

Junninen, H., Ehn, M., Petäjä, T., Luosujärvi, L., Kotiaho, T., Kostiainen, R., Rohner, U., Gonin, M., Fuhrer, K., Kulmala, M., and Worsnop, D. R.: A high-resolution mass spectrometer to measure atmospheric ion composition, Atmos. Meas. Tech., 3, 1039-1053, https://doi.org/10.5194/amt-3-1039-2010, 2010.

Krapf, M., Kunzi, L., Allenbach, S., Bruns, E. A., Gavarini, I., El-Haddad, I., Slowik, J. G., Prevot, A. S. H., Drinovec, L., Mocnik, G., Dumbgen, L., Salathe, M., Baumlin, N., Sioutas, C., Baltensperger, U., Dommen, J., and Geiser, M.: Wood combustion particles induce adverse effects to normal and diseased airway epithelia, Environ Sci-Proc Imp, 19, 538-548, https://doi.org/10.1039/c6em00586a, 2017.

Kuang, Y., He, Y., Xu, W., Yuan, B., Zhang, G., Ma, Z., Wu, C., Wang, C., Wang, S., Zhang, S., Tao, J., Ma, N., Su, H., Cheng, Y., Shao, M., and Sun, Y.: Photochemical Aqueous-Phase Reactions Induce Rapid Daytime Formation of Oxygenated Organic Aerosol on the North China Plain, Environ Sci Technol, https://doi.org/10.1021/acs.est.9b06836, 2020.

Laden, F., Schwartz, J., Speizer, F. E., and Dockery, D. W.: Reduction in fine particulate air pollution and mortality - Extended follow-up of the Harvard six cities study, Am J Resp Crit Care, 173, 667-672, https://doi.org/10.1164/rccm.200503-443OC, 2006.

Lamkaddam, H., Dommen, J., Ranjithkumar, A., Gordon, H., Wehrle, G., Krechmer, J., Majluf, F., Salionov, D., Schmale, J., Bjelić, S., Carslaw, K. S., El Haddad, I., and Baltensperger, U.: Large contribution to secondary organic aerosol from isoprene cloud chemistry, Science Advances, 7, eabe2952, https://doi.org/10.1126/sciadv.abe2952, 2021.

Lanz, V. A., Alfarra, M. R., Baltensperger, U., Buchmann, B., Hueglin, C., and Prévôt, A. S. H.: Source apportionment of submicron organic aerosols at an urban site by factor analytical modelling of aerosol mass spectra, Atmos. Chem. Phys., 7, 1503-1522, https://doi.org/10.5194/acp-7-1503-2007, 2007.

Larsen, R. J., and Marx, M. L.: An introduction to mathematical statistics and its applications, Sixth edition. ed., Pearson, Boston, MA, USA, 2018.

Legrand, M., Preunkert, S., Galy-Lacaux, C., Liousse, C., and Wagenbach, D.: Atmospheric year-round records of dicarboxylic acids and sulfate at three French sites located between 630 and 4360 m elevation, J Geophys Res-Atmos, 110, D13302, https://doi.org/10.1029/2004JD005515, 2005.

Li, N., Sioutas, C., Cho, A., Schmitz, D., Misra, C., Sempf, J., Wang, M. Y., Oberley, T., Froines, J., and Nel, A.: Ultrafine particulate pollutants induce oxidative stress and mitochondrial damage, Environ Health Persp, 111, 455-460, https://doi.org/10.1289/ehp.6000, 2003.

Liu, F., Ronald, J. V., Eskes, H., Ding, J. Y., and Mijling, B.: Evaluation of modeling NO_2 concentrations driven by satellite-derived and bottom-up emission inventories using in situ measurements over China, Atmos Chem Phys, 18, 4171-4186, https://doi.org/10.5194/acp-18-4171-2018, 2018.

Liu, J. C., Wilson, A., Mickley, L. J., Dominici, F., Ebisu, K., Wang, Y., Sulprizio, M. P., Peng, R. D., Yue, X., Son, J. Y., Anderson, G. B., and Bell, M. L.: Wildfire-specific Fine Particulate Matter and Risk of Hospital Admissions in Urban and Rural Counties, Epidemiology, 28, 77-85, https://doi.org/10.1097/EDE.0000000000000556, 2017a.

Liu, T., Li, Z., Chan, M., and Chan, C. K.: Formation of secondary organic aerosols from gas-phase emissions of heated cooking oils, Atmos. Chem. Phys., 17, 7333-7344, https://doi.org/10.5194/acp-17-7333-2017, 2017b.

Lohmann, U., and Feichter, J.: Global indirect aerosol effects: a review, Atmos Chem Phys, 5, 715-737, https://doi.org/10.5194/acp-5-715-2005, 2005.

Lopez-Hilfiker, F. D., Mohr, C., Ehn, M., Rubach, F., Kleist, E., Wildt, J., Mentel, T. F., Lutz, A., Hallquist, M., Worsnop, D., and Thornton, J. A.: A novel method for online analysis of gas and particle composition:

description and evaluation of a Filter Inlet for Gases and AEROsols (FIGAERO), Atmos. Meas. Tech., 7, 983-1001, https://doi.org/10.5194/amt-7-983-2014, 2014.

Lopez-Hilfiker, F. D., Pospisilova, V., Huang, W., Kalberer, M., Mohr, C., Stefenelli, G., Thornton, J. A., Baltensperger, U., Prevot, A. S. H., and Slowik, J. G.: An extractive electrospray ionization time-of-flight mass spectrometer (EESI-TOF) for online measurement of atmospheric aerosol particles, Atmos Meas Tech, 12, 4867-4886, https://doi.org/10.5194/amt-12-4867-2019, 2019.

Mayer, H.: Air pollution in cities, Atmospheric Environment, 33, 4029-4037, https://doi.org/10.1016/S1352-2310(99)00144-2, 1999.

Mehra, A., Wang, Y., Krechmer, J. E., Lambe, A., Majluf, F., Morris, M. A., Priestley, M., Bannan, T. J., Bryant, D. J., Pereira, K. L., Hamilton, J. F., Rickard, A. R., Newland, M. J., Stark, H., Croteau, P., Jayne, J. T., Worsnop, D. R., Canagaratna, M. R., Wang, L., and Coe, H.: Evaluation of the chemical composition of gas- and particle-phase products of aromatic oxidation, Atmos. Chem. Phys., 20, 9783-9803, https://doi.org/10.5194/acp-20-9783-2020, 2020.

Middlebrook, A. M., Bahreini, R., Jimenez, J. L., and Canagaratna, M. R.: Evaluation of Composition-Dependent Collection Efficiencies for the Aerodyne Aerosol Mass Spectrometer using Field Data, Aerosol Sci Tech, 46, 258-271, https://doi.org/10.1080/02786826.2011.620041, 2012.

Mohr, C., DeCarlo, P. F., Heringa, M. F., Chirico, R., Slowik, J. G., Richter, R., Reche, C., Alastuey, A., Querol, X., Seco, R., Penuelas, J., Jimenez, J. L., Crippa, M., Zimmermann, R., Baltensperger, U., and Prevot, A. S. H.: Identification and quantification of organic aerosol from cooking and other sources in Barcelona using aerosol mass spectrometer data, Atmos Chem Phys, 12, 1649-1665, https://doi.org/10.5194/acp-12-1649-2012, 2012.

Mohr, C., Lopez-Hilfiker, F. D., Zotter, P., Prévôt, A. S., Xu, L., Ng, N. L., Herndon, S. C., Williams, L. R., Franklin, J. P., and Zahniser, M. S.: Contribution of nitrated phenols to wood burning brown carbon light absorption in Detling, United Kingdom during winter time, Environ Sci Technol, 47, 6316-6324, https://doi.org/10.1021/es400683v, 2013.

Muller, M., Eicher, P., D'Anna, B., Tan, W., and Wisthaler, A.: Direct Sampling and Analysis of Atmospheric Particulate Organic Matter by Proton-Transfer-Reaction Mass Spectrometry, Anal Chem, 89, 10889-10897, https://doi.org/10.1021/acs.analchem.7b02582, 2017.

Myhre, G., Shindell, D., Bréon, F.-M., Collins, W., Fuglestvedt, J., Huang, J., Koch, D., Lamarque, J.-F., Lee, D., Mendoza, B., Nakajima, T., Robock, A., Stephens, G., Takemura, T., and Zhang, H.: Anthropogenic and Natural Radiative Forcing. In: Climate Change 2013: The Physical Science Basis. Contribution of Working Group I to the Fifth Assessment Report of the Intergovernmental Panel on Climate Change [Stocker, T.F., Qin, D., Plattner, G.-K., Tignor, M., Allen, S.K., Boschung, J., Nauels, A., Xia, Y., Bex, V. and Midgley, P.M. (eds.)]. Cambridge University Press, Cambridge, United Kingdom and New York, NY, USA, 2013.

Ng, N. L., Canagaratna, M. R., Jimenez, J. L., Zhang, Q., Ulbrich, I. M., and Worsnop, D. R.: Real-Time Methods for Estimating Organic Component Mass Concentrations from Aerosol Mass Spectrometer Data, Environ Sci Technol, 45, 910-916, https://doi.org/10.1021/es102951k, 2011.

Paatero, P.: Least squares formulation of robust non-negative factor analysis, Chemometr Intell Lab, 37, 23-35, https://doi.org/10.1016/S0169-7439(96)00044-5, 1997.

Paatero, P., and Hopke, P. K.: Discarding or downweighting high-noise variables in factor analytic models, Anal Chim Acta, 490, 277-289, https://doi.org/10.1016/S0003-2670(02)01643-4, 2003.

Paatero, P., Eberly, S., Brown, S. G., and Norris, G. A.: Methods for estimating uncertainty in factor analytic solutions, Atmos Meas Tech, 7, 781-797, https://doi.org/10.5194/amt-7-781-2014, 2014.

Penner, J. E., Xu, L., and Wang, M. H.: Satellite methods underestimate indirect climate forcing by aerosols, P Natl Acad Sci USA, 108, 13404-13408, https://doi.org/10.1073/pnas.1018526108, 2011.

Petit, J. E., Favez, O., Albinet, A., and Canonaco, F.: A user-friendly tool for comprehensive evaluation of the geographical origins of atmospheric pollution: Wind and trajectory analyses, Environ Modell Softw, 88, 183-187, https://doi.org/10.1016/j.envsoft.2016.11.022, 2017.

Pieber, S. M., El Haddad, I., Slowik, J. G., Canagaratna, M. R., Jayne, J. T., Platt, S. M., Bozzetti, C., Daellenbach, K. R., Frohlich, R., Vlachou, A., Klein, F., Dommen, J., Miljevic, B., Jimenez, J. L., Worsnop, D. R., Baltensperger, U., and Prevot, A. S. H.: Inorganic Salt Interference on CO_2^+ in Aerodyne AMS and ACSM Organic Aerosol Composition Studies, Environ Sci Technol, 50, 10494-10503, https://doi.org/10.1021/acs.est.6b01035, 2016.

Pope, C. A., Burnett, R. T., Thun, M. J., Calle, E. E., Krewski, D., Ito, K., and Thurston, G. D.: Lung cancer, cardiopulmonary mortality, and long-term exposure to fine particulate air pollution, Jama-J Am Med Assoc, 287, 1132-1141, https://doi.org/10.1001/jama.287.9.1132, 2002.

Qi, L., Chen, M. D., Stefenelli, G., Pospisilova, V., Tong, Y. D., Bertrand, A., Hueglin, C., Ge, X. L., Baltensperger, U., Prevot, A. S. H., and Slowik, J. G.: Organic aerosol source apportionment in Zurich using an extractive electrospray ionization time-of-flight mass spectrometer (EESI-TOF-MS) - Part 2: Biomass burning influences in winter, Atmos Chem Phys, 19, 8037-8062, https://doi.org/10.5194/acp-19-8037-2019, 2019.

Reuter, S., Gupta, S. C., Chaturvedi, M. M., and Aggarwal, B. B.: Oxidative stress, inflammation, and cancer How are they linked?, Free Radical Bio Med, 49, 1603-1616, https://doi.org/10.1016/j.freeradbiomed.2010.09.006, 2010.

Rolph, G., Stein, A., and Stunder, B.: Real-time Environmental Applications and Display sYstem: READY, Environ Modell Softw, 95, 210-228, https://doi.org/10.1016/j.envsoft.2017.06.025, 2017.

Sellegri, K., Laj, P., Marinoni, A., Dupuy, R., Legrand, M., and Preunkert, S.: Contribution of gaseous and particulate species to droplet solute composition at the Puy de Dome, France, Atmos Chem Phys, 3, 1509-1522, https://doi.org/10.5194/acp-3-1509-2003, 2003.

Sempere, R., and Kawamura, K.: Comparative Distributions of Dicarboxylic-Acids and Related Polar Compounds in Snow Rain and Aerosols from Urban Atmosphere, Atmospheric Environment, 28, 449-459, https://doi.org/10.1016/1352-2310(94)90123-6, 1994.

Shen, V. K., Siderius, D. W., Krekelberg, W. P., and Hatch, H. W.: NIST standard reference simulation website, NIST Standard Reference Database, 2014-2017, https://doi.org/10.18434/T4M88Q, 2017.

Stefenelli, G., Bertrand, A., Yuan, B., Qi, L., Pospisilova, V., Lopez-Hilfiker, F. D., Hueglin, C., Baltensperger, U., Prévôt, A. S. H., and Slowik, J. G.: Laboratory and field investigation of biomass burning aerosol aging using an extractive electrospray ionization time-of-flight mass spectrometer (EESI-TOF), *in preparation*.

Stefenelli, G., Pospisilova, V., Lopez-Hilfiker, F. D., Daellenbach, K. R., Hüglin, C., Tong, Y., Baltensperger, U., Prévôt, A. S. H., and Slowik, J. G.: Organic aerosol source apportionment in Zurich using an extractive electrospray ionization time-of-flight mass spectrometer (EESI-TOF-MS) – Part 1: Biogenic influences and day–night chemistry in summer, Atmos. Chem. Phys., 19, 14825-14848, https://doi.org/10.5194/acp-19-14825-2019, 2019.

Stein, A. F., Draxler, R. R., Rolph, G. D., Stunder, B. J. B., Cohen, M. D., and Ngan, F.: Noaa's Hysplit Atmospheric Transport and Dispersion Modeling System, B Am Meteorol Soc, 96, 2059-2077, https://doi.org/10.1175/BAMS-D-14-00110.1, 2015.

Sun, Y. L., Zhang, Q., Schwab, J. J., Demerjian, K. L., Chen, W. N., Bae, M. S., Hung, H. M., Hogrefe, O., Frank, B., Rattigan, O. V., and Lin, Y. C.: Characterization of the sources and processes of organic and inorganic aerosols in New York city with a high-resolution time-of-flight aerosol mass apectrometer, Atmos. Chem. Phys., 11, 1581-1602, https://doi.org/10.5194/acp-11-1581-2011, 2011.

Sun, Y. L., Wang, Z. F., Fu, P. Q., Yang, T., Jiang, Q., Dong, H. B., Li, J., and Jia, J. J.: Aerosol composition, sources and processes during wintertime in Beijing, China, Atmos. Chem. Phys., 13, 4577-4592, https://doi.org/10.5194/acp-13-4577-2013, 2013.

Sun, Y. L., Du, W., Fu, P. Q., Wang, Q. Q., Li, J., Ge, X. L., Zhang, Q., Zhu, C. M., Ren, L. J., Xu, W. Q., Zhao, J., Han, T. T., Worsnop, D. R., and Wang, Z. F.: Primary and secondary aerosols in Beijing in winter: sources, variations and processes, Atmos Chem Phys, 16, 8309-8329, https://doi.org/10.5194/acp-16-8309-2016, 2016a.

Sun, Y. L., Wang, Z. F., Wild, O., Xu, W. Q., Chen, C., Fu, P. Q., Du, W., Zhou, L. B., Zhang, Q., Han, T. T., Wang, Q. Q., Pan, X. L., Zheng, H. T., Li, J., Guo, X. F., Liu, J. G., and Worsnop, D. R.: "APEC Blue": Secondary Aerosol Reductions from Emission Controls in Beijing, Sci Rep-Uk, 6, 20668, https://doi.org/10.1038/srep20668 (2016), 2016b.

Tan, Y., Carlton, A. G., Seitzinger, S. P., and Turpin, B. J.: SOA from methylglyoxal in clouds and wet aerosols: Measurement and prediction of key products, Atmospheric Environment, 44, 5218-5226, https://doi.org/10.1016/j.atmosenv.2010.08.045, 2010.

Tan, Y., Lim, Y., Altieri, K., Seitzinger, S., and Turpin, B.: Mechanisms leading to oligomers and SOA through aqueous photooxidation: insights from OH radical oxidation of acetic acid and methylglyoxal, Atmos Chem Phys, 12, 801, https://doi.org/10.5194/acp-12-801-2012, 2012.

Ulbrich, I. M., Canagaratna, M. R., Zhang, Q., Worsnop, D. R., and Jimenez, J. L.: Interpretation of organic components from Positive Matrix Factorization of aerosol mass spectrometric data, Atmos Chem Phys, 9, 2891-2918, https://doi.org/10.5194/acp-9-2891-2009, 2009.

Wang, S., Newland, M. J., Deng, W., Rickard, A. R., Hamilton, J. F., Muñoz, A., Ródenas, M., Vázquez, M. M., Wang, L., and Wang, X.: Aromatic Photo-oxidation, A New Source of Atmospheric Acidity, Environ Sci Technol, 54, 7798-7806, https://doi.org/10.1021/acs.est.0c00526, 2020.

Wang, Y., Hu, M., Wang, Y., Zheng, J., Shang, D., Yang, Y., Liu, Y., Li, X., Tang, R., Zhu, W., Du, Z., Wu, Y., Guo, S., Wu, Z., Lou, S., Hallquist, M., and Yu, J. Z.: The formation of nitro-aromatic compounds under high NOx and anthropogenic VOC conditions in urban Beijing, China, Atmos. Chem. Phys., 19, 7649-7665, https://doi.org/10.5194/acp-19-7649-2019, 2019.

Williams, B. J., Goldstein, A. H., Kreisberg, N. M., and Hering, S. V.: An In-Situ Instrument for Speciated Organic Composition of Atmospheric Aerosols: Thermal Desorption Aerosol GC/MS-FID (TAG), Aerosol Sci Tech, 40, 627-638, https://doi.org/10.1080/02786820600754631, 2006.

Williams, L. R., Gonzalez, L. A., Peck, J., Trimborn, D., McInnis, J., Farrar, M. R., Moore, K. D., Jayne, J. T., Robinson, W. A., Lewis, D. K., Onasch, T. B., Canagaratna, M. R., Trimborn, A., Timko, M. T., Magoon, G., Deng, R., Tang, D., Blanco, E. D. L. R., Prevot, A. S. H., Smith, K. A., and Worsnop, D. R.: Characterization of an aerodynamic lens for transmitting particles greater than 1 micrometer in diameter into the Aerodyne aerosol mass spectrometer, Atmos Meas Tech, 6, 3271-3280, https://doi.org/10.5194/amt-6-3271-2013, 2013.

Xing, L., Wu, J., Elser, M., Tong, S., Liu, S., Li, X., Liu, L., Cao, J., Zhou, J., El-Haddad, I., Huang, R., Ge, M., Tie, X., Prévôt, A. S. H., and Li, G.: Wintertime secondary organic aerosol formation in Beijing–Tianjin–Hebei (BTH): contributions of HONO sources and heterogeneous reactions, Atmos. Chem. Phys., 19, 2343-2359, https://doi.org/10.5194/acp-19-2343-2019, 2019.

Xu, S. S., Liu, W. X., and Tao, S.: Emission of polycyclic aromatic hydrocarbons in China, Environ Sci Technol, 40, 702-708, https://doi.org/10.1021/es0517062, 2006.

Xu, W. Q., Sun, Y. L., Wang, Q. Q., Zhao, J., Wang, J. F., Ge, X. L., Xie, C. H., Zhou, W., Du, W., Li, J., Fu, P. Q., Wang, Z. F., Worsnop, D. R., and Coe, H.: Changes in Aerosol Chemistry From 2014 to 2016 in Winter in Beijing: Insights From High-Resolution Aerosol Mass Spectrometry, J Geophys Res-Atmos, 124, 1132-1147, https://doi.org/10.1029/2018JD029245, 2019.

Zaytsev, A., Koss, A. R., Breitenlechner, M., Krechmer, J. E., Nihill, K. J., Lim, C. Y., Rowe, J. C., Cox, J. L., Moss, J., Roscioli, J. R., Canagaratna, M. R., Worsnop, D. R., Kroll, J. H., and Keutsch, F. N.: Mechanistic study of the formation of ring-retaining and ring-opening products from the oxidation of aromatic compounds under urban atmospheric conditions, Atmos. Chem. Phys., 19, 15117-15129, https://doi.org/10.5194/acp-19-15117-2019, 2019.

Zhang, J. K., Sun, Y., Liu, Z. R., Ji, D. S., Hu, B., Liu, Q., and Wang, Y. S.: Characterization of submicron aerosols during a month of serious pollution in Beijing, 2013, Atmos Chem Phys, 14, 2887-2903, https://doi.org/10.5194/acp-14-2887-2014, 2014.

Zhang, Y. X., Schauer, J. J., Zhang, Y. H., Zeng, L. M., Wei, Y. J., Liu, Y., and Shao, M.: Characteristics of particulate carbon emissions from real-world Chinese coal combustion, Environ Sci Technol, 42, 5068-5073, https://doi.org/10.1021/es7022576, 2008.

Zhao, J., Qiu, Y. M., Zhou, W., Xu, W. Q., Wang, J. F., Zhang, Y. J., Li, L. J., Xie, C. H., Wang, Q. Q., Du, W., Worsnop, D. R., Canagaratna, M. R., Zhou, L. B., Ge, X. L., Fu, P. Q., Li, J., Wang, Z. F., Donahue, N. M., and Sun, Y. L.: Organic Aerosol Processing During Winter Severe Haze Episodes in Beijing, J Geophys Res-Atmos, 124, 10248-10263, https://doi.org/10.1029/2019JD030832, 2019.

Zhou, J., Zotter, P., Bruns, E. A., Stefenelli, G., Bhattu, D., Brown, S., Bertrand, A., Marchand, N., Lamkaddam, H., Slowik, J. G., Prévôt, A. S. H., Baltensperger, U., Nussbaumer, T., El-Haddad, I., and Dommen, J.: Particle-bound reactive oxygen species (PB-ROS) emissions and formation pathways in residential wood smoke under different combustion and aging conditions, Atmos. Chem. Phys., 18, 6985-7000, https://doi.org/10.5194/acp-18-6985-2018, 2018.

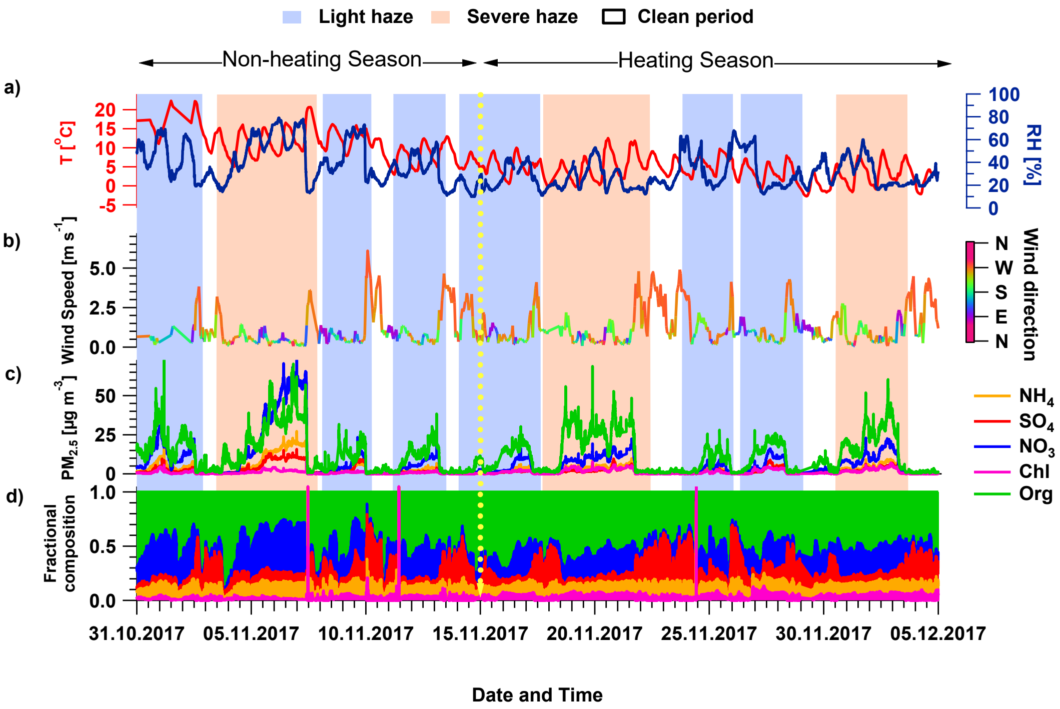

Figure 1. Time series of meteorological variables and NR-PM$_{2.5}$ composition. (a) temperature (*T*) and relative humidity (RH), (b) wind speed and wind direction, (c) mass concentrations of NR-PM$_{2.5}$ species measured by the AMS, and (d) mass fractions of the species shown in Fig. 1c. Shaded area indicates haze episodes: light haze episodes are defined as having NR-PM$_{2.5}$ concentrations from 20 to 150 μg m^{-3} (light blue), while severe haze episodes are defined having NR-PM$_{2.5}$ concentrations above 150 μg m^{-3} (light red).

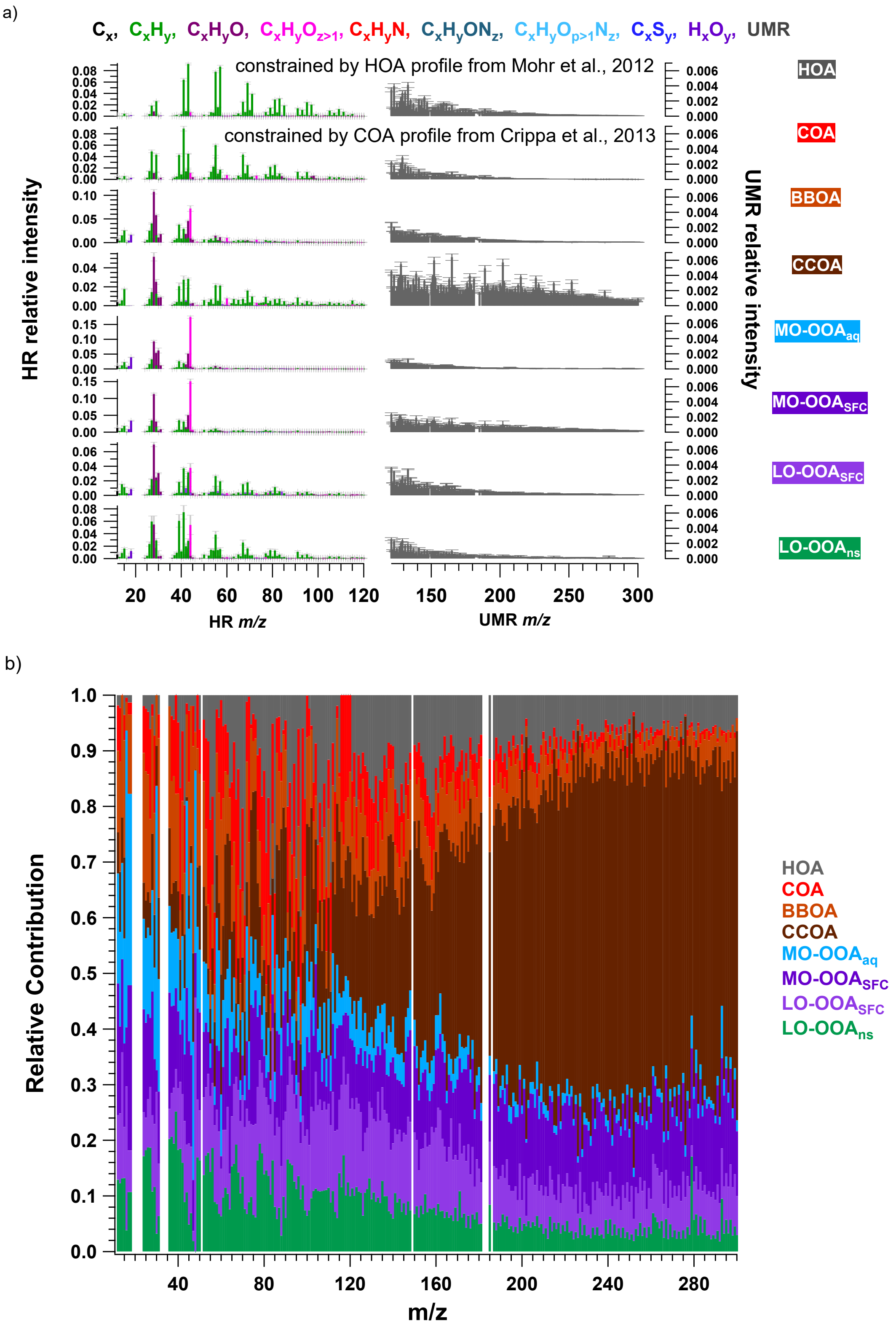

Figure 2. Averaged mass spectra (a) and relative contributions (b) of the 8-factor solution from the AMS PMF bootstrap result. The mass spectra consist of HR ions from *m/z* 12 to 120, and integrated integer *m/z* (denoted UMR) from *m/z* 121 to 300, whose intensity is multiplied by 5. In (a), error bars denote standard deviation calculated from all accepted bootstrap solutions.

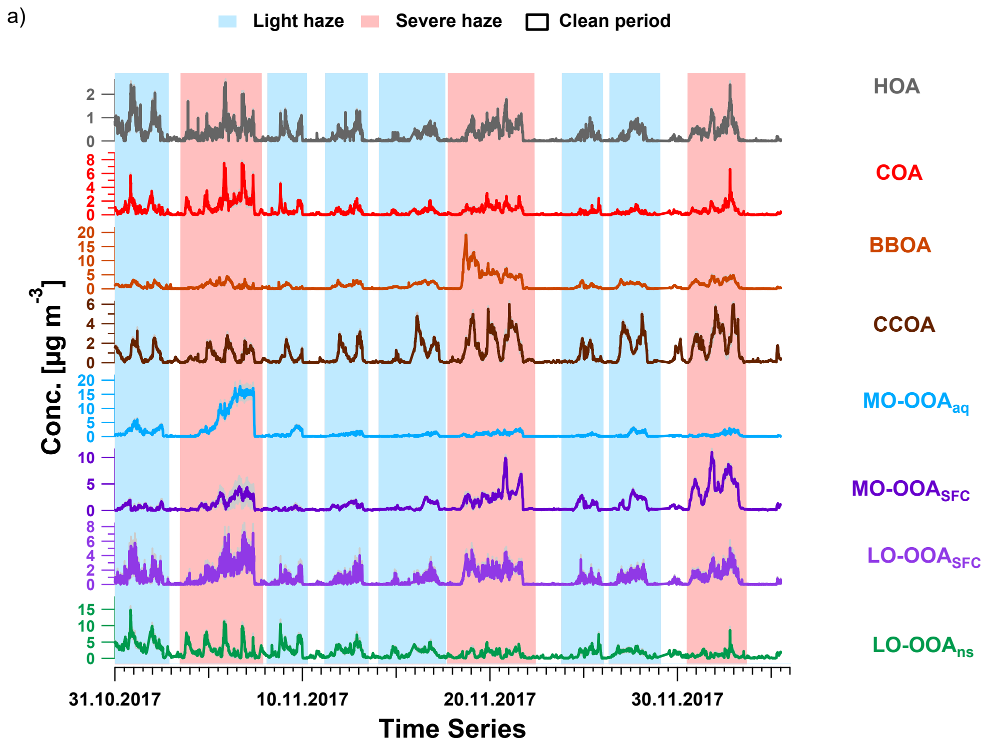
a)
Light haze
Severe haze
Clean period
HOA
COA
BBOA
CCOA
MO-OOA$_{aq}$
MO-OOA$_{SFC}$
LO-OOA$_{SFC}$
LO-OOA$_{ns}$
Conc. [µg m^{-3}]
31.10.2017
10.11.2017
20.11.2017
30.11.2017
Time Series

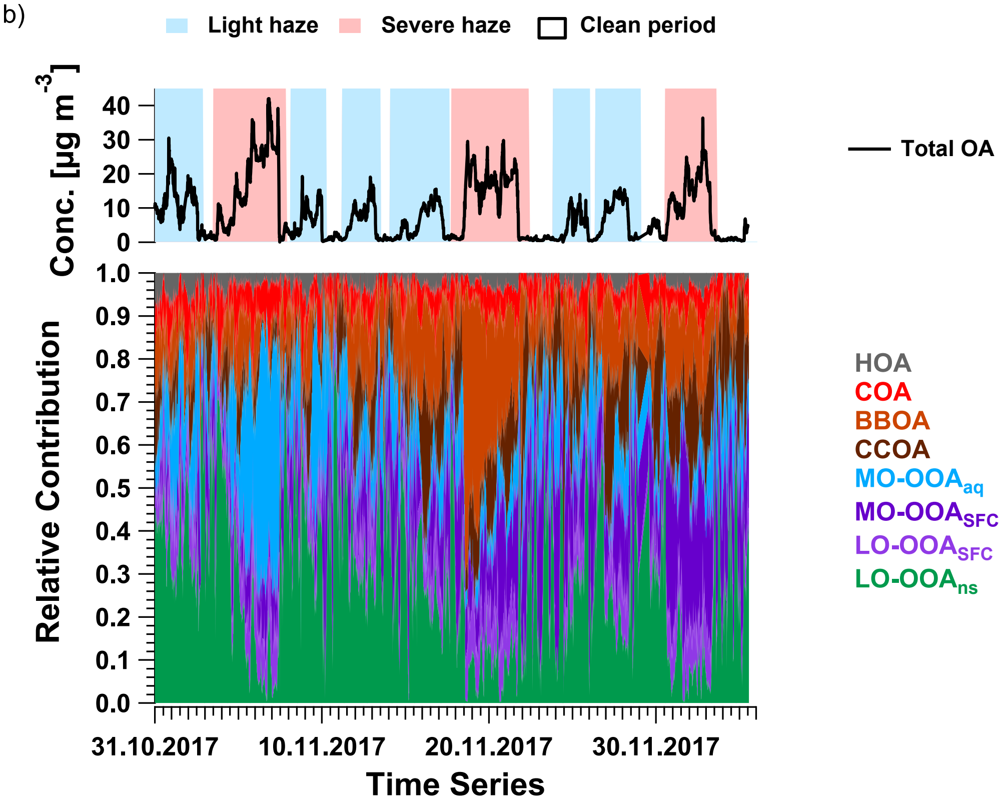
b)
Light haze
Severe haze
Clean period
Total OA
Conc. [µg m^{-3}]
0
10
20
30
40
Relative Contribution
0.0
0.1
0.2
0.3
0.4
0.5
0.6
0.7
0.8
0.9
1.0
HOA
COA
BBOA
CCOA
MO-OOA$_{aq}$
MO-OOA$_{SFC}$
LO-OOA$_{SFC}$
LO-OOA$_{ns}$
31.10.2017
10.11.2017
20.11.2017
30.11.2017
Time Series

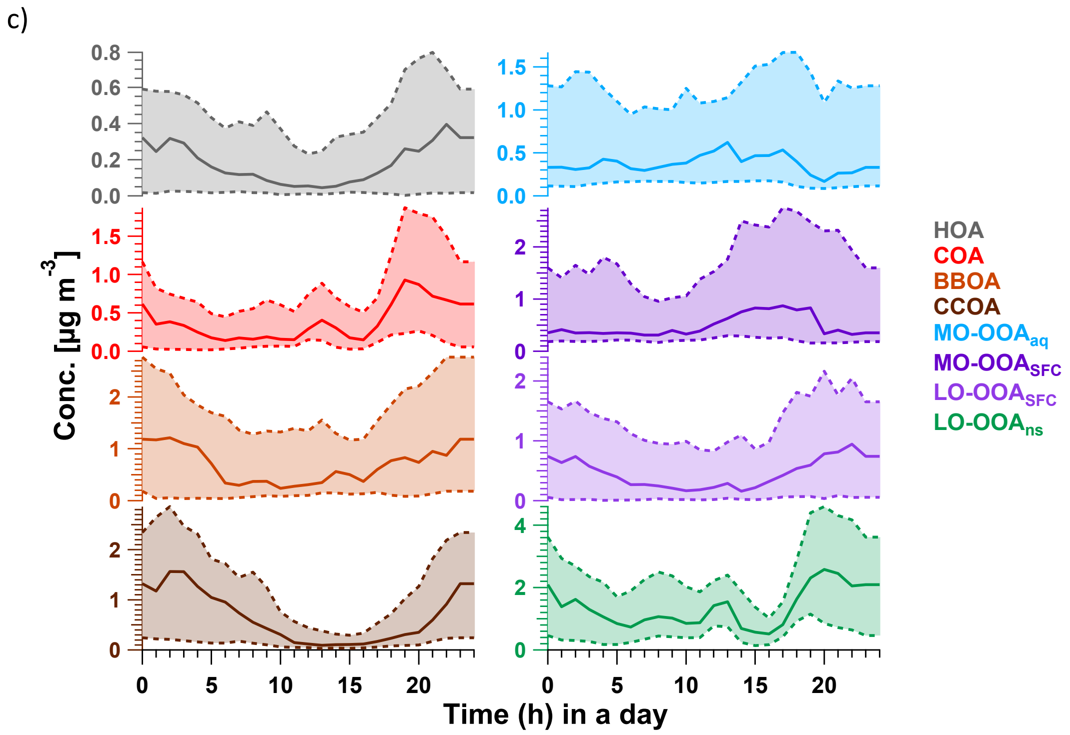

Figure 3. (a) Averaged time series with standard deviations (shaded area with same colour as factor), (b) averaged total OA concentration and relative contributions and (c) median diurnal cycle the accepted AMS PMF bootstrap 8-factor solutions based on the criteria discussed in Sect. 2.3. Lower and upper dashed lines in (c) indicate 1st and 3rd quantiles. In (a) and (b), the shaded areas in red and in blue represent periods of severe haze and light haze, respectively.

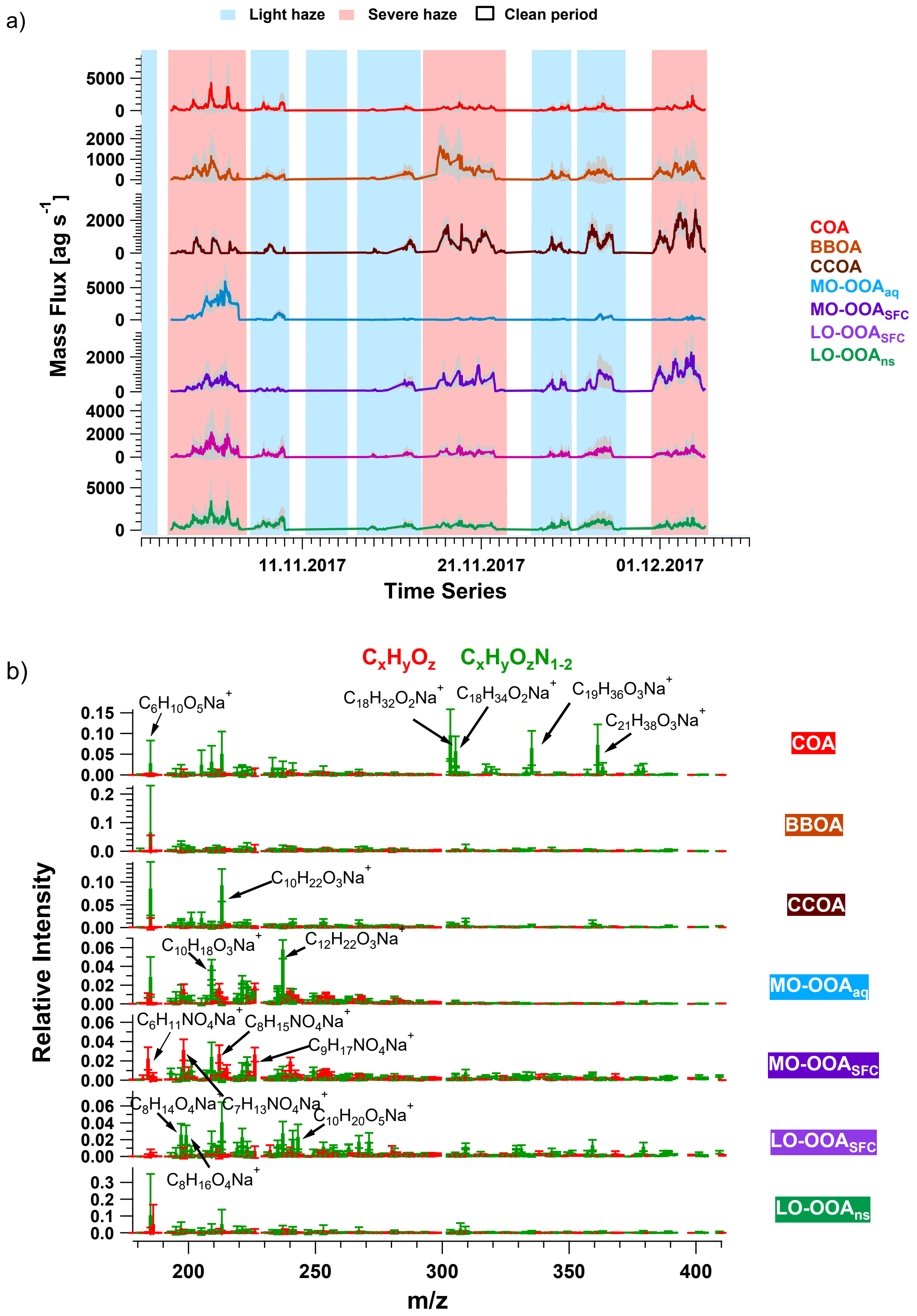

Figure 4. The averaged (a) time series and (b) mass spectra of accepted solutions from combined bootstrap/*a*-value analysis of the EESI-TOF dataset. EESI-TOF time series are constrained by the 7 non-HOA factors retrieved from AMS PMF analysis. Shaded area in (a) indicates the anchor of bootstrap/*a*-value analysis as shown in Eq. (6) and in (b) indicate the standard deviation of each stick calculated from all selected solutions. In (a), the shade area in red and in blue represents severe haze period and light haze period, respectively.

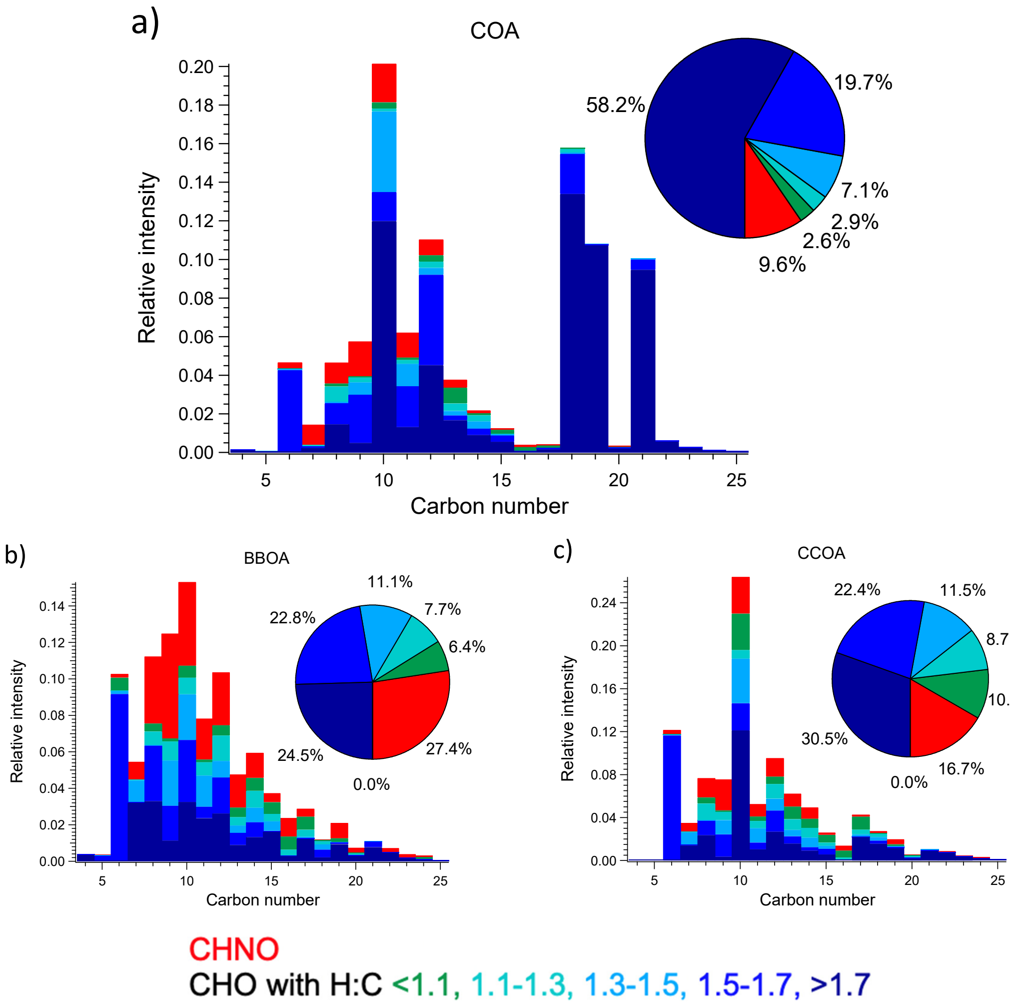

Figure 5. Carbon number distribution plots of three primary factors: (a) COA, (b) BBOA and (c) CCOA, coloured by $C_xH_yO_zN_{1-2}$ and five different $C_xH_yO_z$ categories based on H:C ratio (H:C < 1.1, 1.1 < H:C < 1.3, 1.3 < H:C < 1.5, 1.5 < H:C < 1.7 and H:C > 1.7). Each distribution is normalised such that its sum is 1.

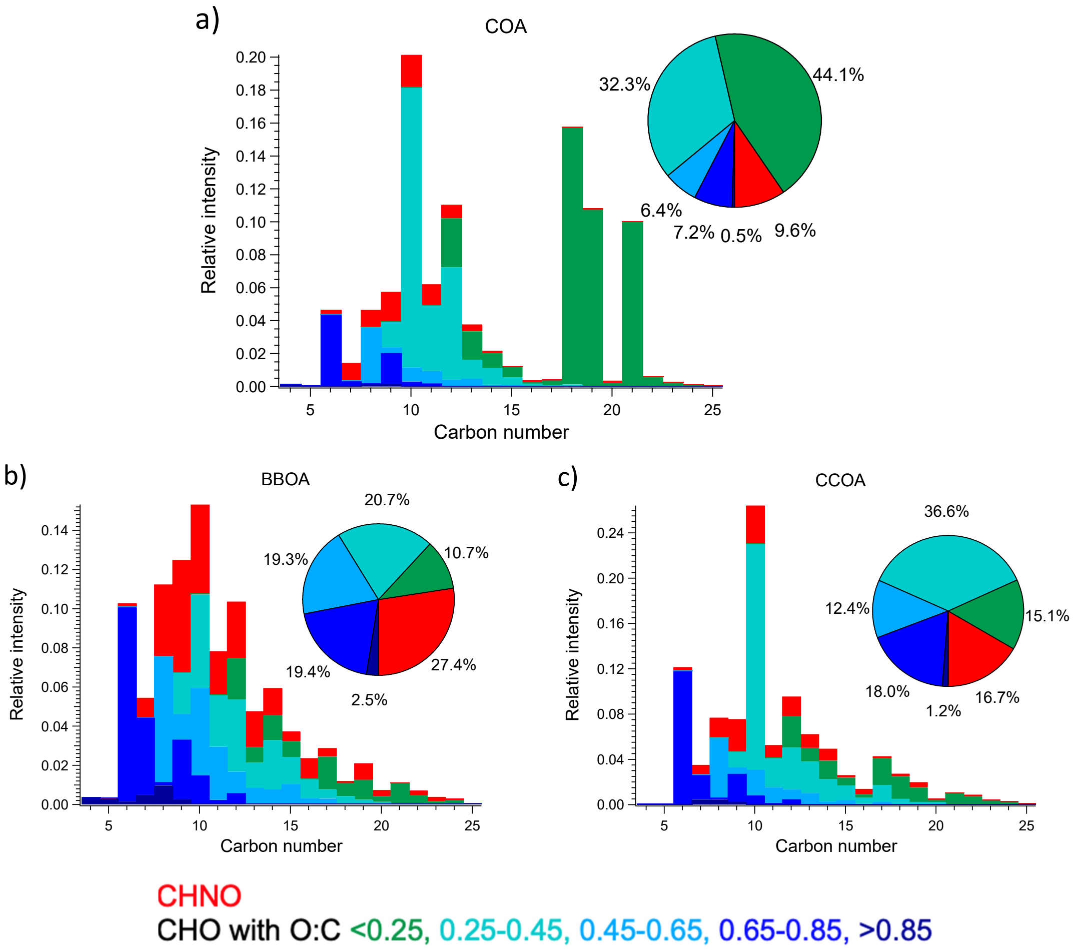

Figure 6. Carbon number distribution plots of three primary factors: (a) COA, (b) BBOA and (c) CCOA, coloured by $C_xH_yO_zN_{1-2}$ and five different $C_xH_yO_z$ categories based on O:C ratio (O:C < 0.25, 0.25 < O:C < 0.45, 0.45 < O:C < 0.65, 0.65 < O:C < 0.85 and O:C > 0.85). Each distribution is normalised such that its sum is 1.

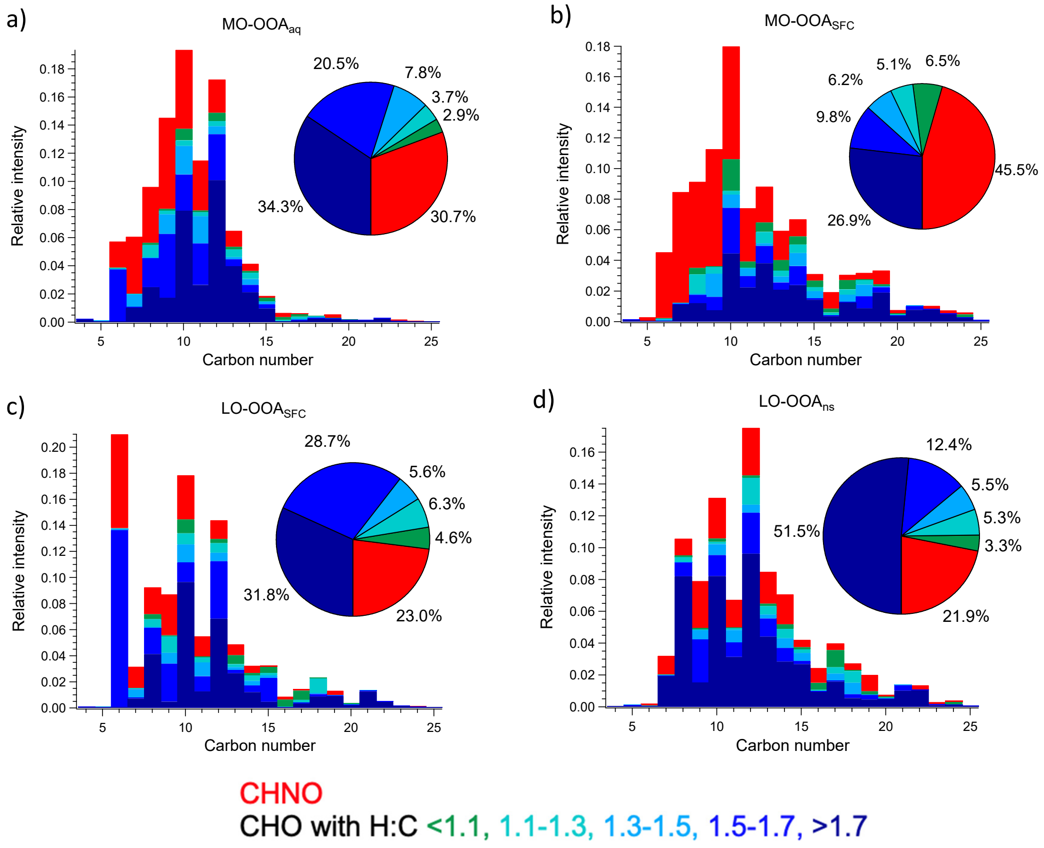

Figure 7. Carbon number distribution plots of four OOA factors: (a) MO-OOA$_{aq}$, (b) MO-OOA$_{SFC}$, (c) LO-OOA$_{SFC}$ and (d) LO-OOA$_{ns}$, coloured by $C_xH_yO_zN_{1-2}$ (red) and five different $C_xH_yO_z$ categories (green to blue) based on H:C ratio (H:C < 1.1, 1.1 < H:C < 1.3, 1.3 < H:C < 1.5, 1.5 < H:C < 1.7 and H:C > 1.7). Each distribution is normalised such that its sum is 1.

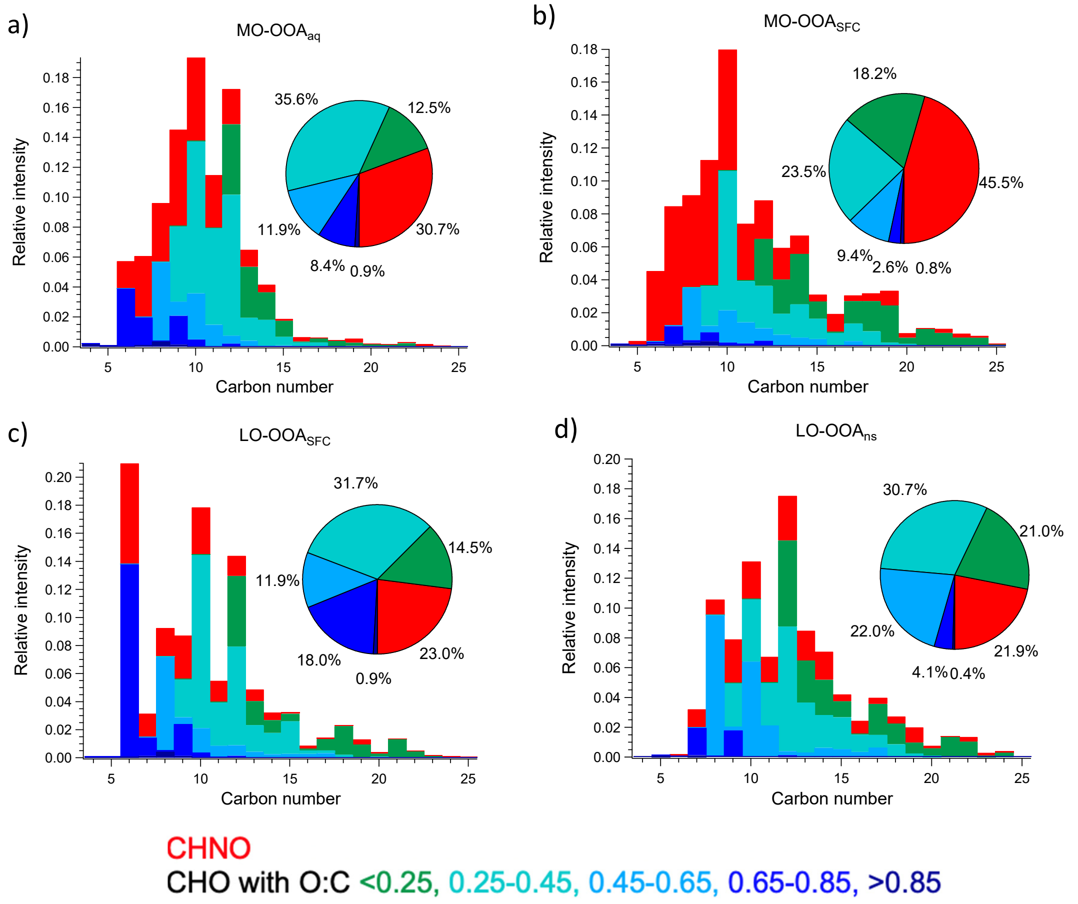

Figure 8. Carbon number distribution plots of four OOA factors: (a) MO-OOA$_{aq}$, (b) MO-OOA$_{SFC}$, (c) LO-OOA$_{SFC}$ and (d) LO-OOA$_{ns}$, coloured by $C_xH_yO_zN_{1-2}$ (red) and five different $C_xH_yO_z$ categories (green to blue) based on O:C ratio (O:C < 0.25, 0.25 < O:C < 0.45, 0.45 < O:C < 0.65, 0.65 < O:C < 0.85 and O:C > 0.85). Each distribution is normalised such that its sum is 1.

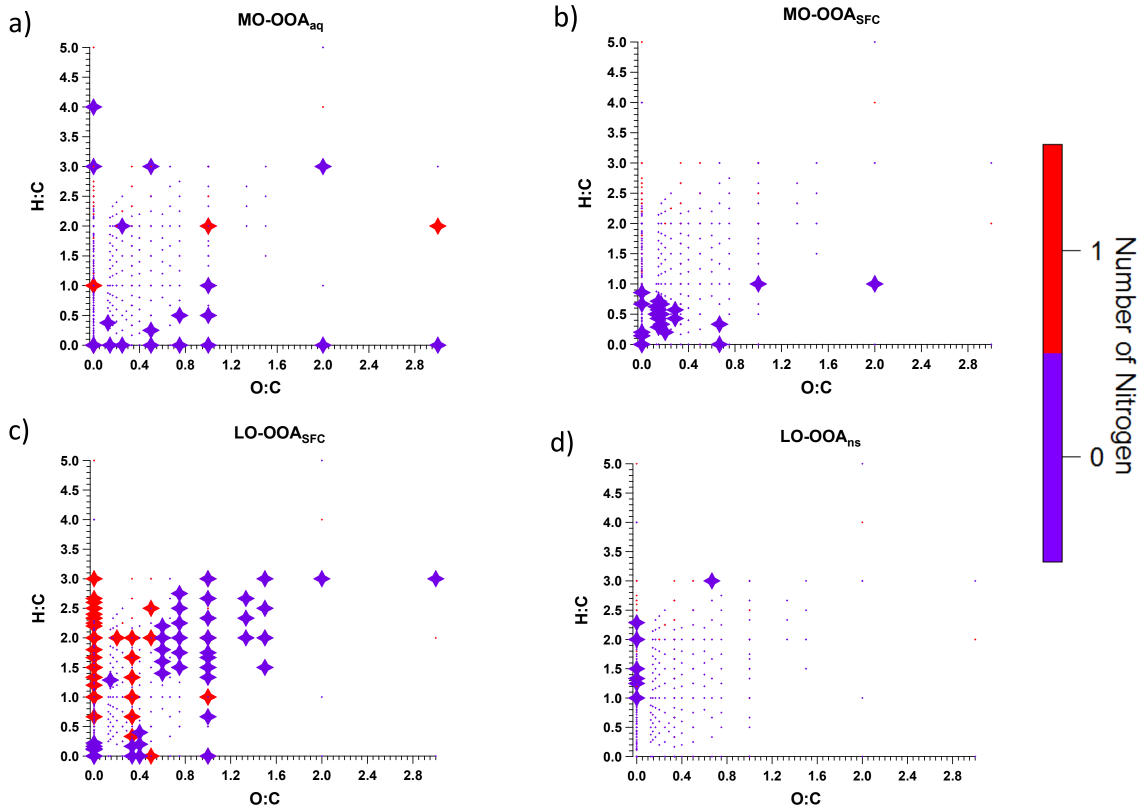

Figure 9. Van Krevelen plot of AMS factor mass spectra for (a) MO-OOA$_{aq}$, (b) MO-OOA$_{SFC}$, (c) LO-OOA$_{SFC}$ and (d) LO-OOA$_{ns}$, coloured by the number of nitrogen atoms. Large symbols denote ions with median z-score ≥ 1.5 and small symbols denotes median z-score < 1.5 for accepted runs from bootstrap analysis.

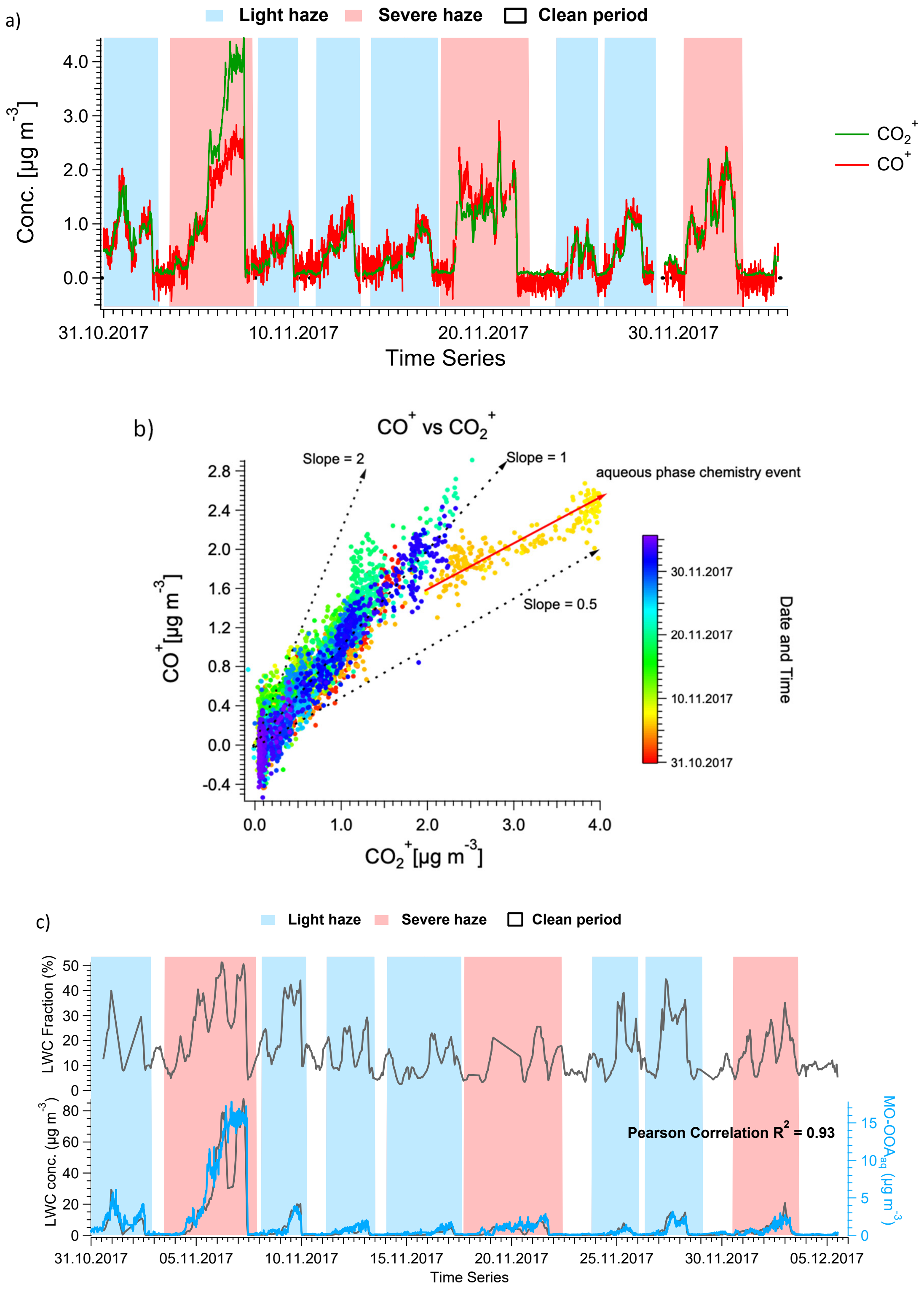

Figure 10. **(a) Time series of AMS-measured CO^+ and CO_2^+ throughout the campaign after CO^+ and CO_2^+ being corrected according to Pieber et al. (2016) and (b) scatter plot of CO^+ and CO_2^+ indicating a different slope for the haze event between 4 November to 7 November 2017, suggesting aqueous phase chemistry may happen in this period. (c) Time series of LWC, both in fraction (top) and mass concentration (bottom), complemented by MO-OOA$_{aq}$, demonstrating the high correlation between the latter two variables. In (a) and (c), the shaded area in red and in blue represents severe haze period and light haze period, respectively.**

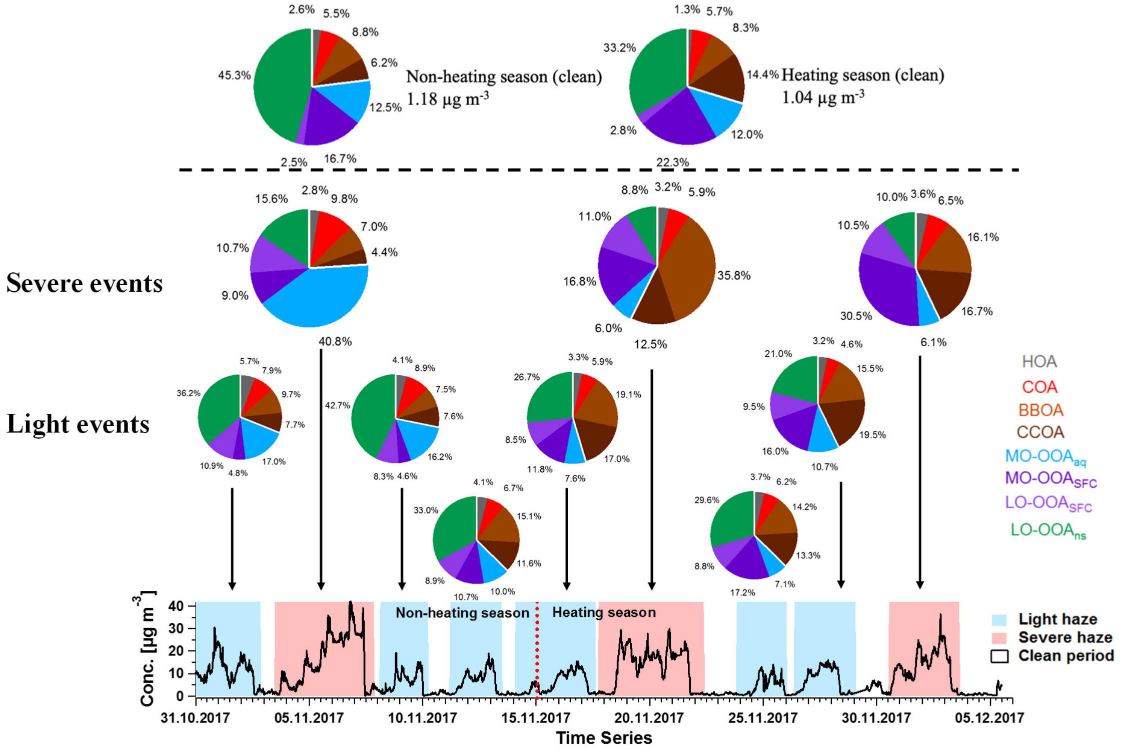

Figure 11. Time series of total OA and the mean contribution of eight AMS factors in each haze event and clean periods for the non-heating and heating periods. The top two pie charts indicate the averaged contributions for clean periods in non-heating season and heating season, three middle and six bottom pie charts indicate corresponding the averaged contributions for three severe haze events (shaded red area) and six light haze events (shaded blue area) according to time series of total OA below, respectively.

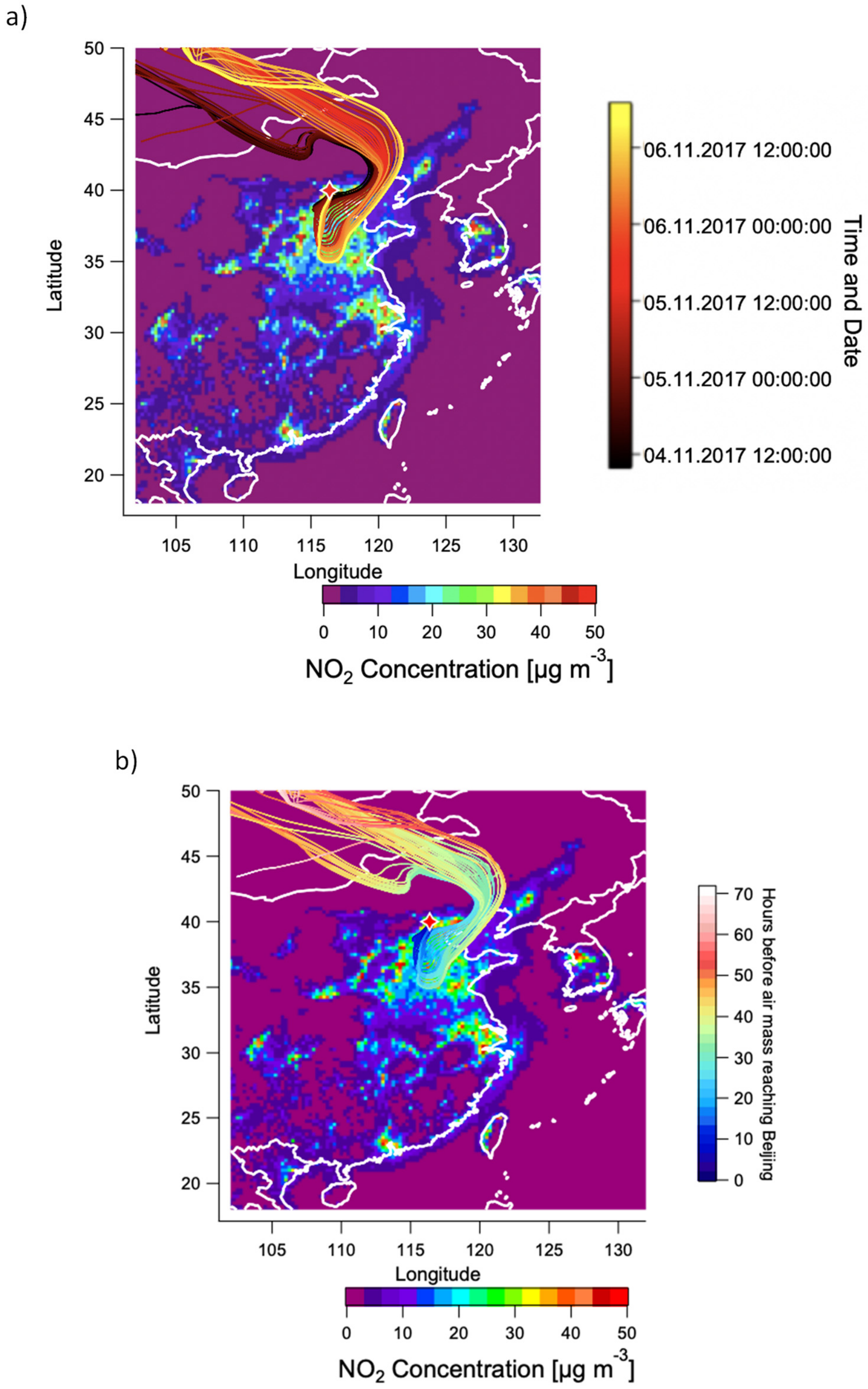

Figure 12. Airmass trajectory analysis. (a) 72-h back-trajectories (HYSPLIT) for the haze event from 4 to 7 November colour-coded by date and time, (b) 72-h back-trajectories for the haze event from 4 to 7 November colour-coded by hours before the air mass reaches Beijing. In both figures, trajectories are overlaid on a 2015 map of surface NO_2 concentrations based on the CHIMERE model and driven by the 2015 DECSO inventory (Liu et al., 2018).